UNIVERSITY OF LIÈGE
Faculty of Applied Science

MASTER'S THESIS

STRUCTURAL ANALYSIS OF A BLENDED WING BODY COMPOSITE AIRCRAFT

Final thesis made towards obtaining the Master's degree in Aerospace Engineering by **Cédric Delvoie**

Supervisor: Ludovic Noels

ACADEMIC YEAR
2015 − 2016
2nd Master in Aerospace Engineering

Acknowledgments

I would like to thank all of the people who have contributed to the culmination of this Master's thesis.

I think especially about Mr. Noels who guided me during the whole project and has always been open to my interrogations.

Mr Andrianne who proposed me this subject, introduced me to Mr. Vigano and Mr. Ernst and helped me to perform the experimental tests of the drone.

Mr. Vigano and Mr. Ernst who have helped me the whole year, and who have make everything which was possible to make my work easier.

Mr Ruffoni and Ms Zorzetto who helped me to perform the three point-bending tests by opening the door of their laboratory to me.

The staff from Refitech who answered my questions about the composite material and who sent me the composite sheet used for the samples.

Abstract

This Master's thesis consists in the structural analysis of a fixed-wing composite unmanned aerial vehicle. The analysis of the aircraft is done in a few steps. The carbon fiber composite used for the skin of the plane is studied thanks to a three point bending test and a finite element model. Then a finite element model of the whole aircraft is developed and is verified thanks to an experimental test. The behavior of the drone performing a resource is studied to ensure that it resists to the maximum aerodynamic loads. In order to do that, an estimation of the aerodynamic loads is performed and a panel method software is used to find the distribution of the pressure all over the aircraft. The results show that the skin of the wing is undergoing small stresses compared to its resistance except at the junction with the winglet.

This paper describes all of the methodology used as well as the material and the tools used and an interpretation of the results.

Contents

List of Figures

Chapter 1

Introduction

When people hear talking about drones, they immediately imagine a quadricopter or a military aircraft. The Guardian Eye is totally different, it is a blended wing body composite aircraft designed for long run missions. It has been originally developed by the company Aircraft Traders Belgium to survey the Savannah in Africa but its usage can vary. It can be equipped with different kind of camera like a high-resolution one or an infra-red captor. The payload of the drone can be adapted to the mission it has to fulfill which makes the Guardian Eye a very versatile unmanned aerial vehicle (UAV).

At first, the UAV was manufactured by Mr Jean-François Stelet who is a craftsman specialized in composite materials. Mass production wasn't possible in that way so the society Refitech has been selected to manufacture it. The development of the drone has been made by trial and error until autumn 2015 and no engineering study has been made concerning the loads applied on the structure in flight neither on the resistance of the structure.

This company decided to use a T700S carbon fiber composite for the skin of the fuselage and the wings. The usage of composite materials has exploded in the last decade its great mechanical proprieties allows to build light and resistant structures. However, working with composite materials is hard as the proprieties of the material can change drastically because of impurities or imperfections.
The wings are filled with a $42kg/m^3$ polyurethane foam. Using foam instead of stingers is also an interesting technique which allows to save weight for small aircrafts.
The structure and the material used are crucial factors in the design of an aircraft. The structure must be able to resist to the highest load that the plane can encounter during the flight but it also needs to be as light as possible to ensure great performances.

This thesis addresses different subjects which will lead to the final analysis of the structure in a flight configuration on a finite element model.

- First of all, the behavior of the composite materials has to be studied in order to use the good proprieties of the material in the finite element software.

- The second objective is to build a finite element model of the plane which is representative of the reality

- The aerodynamics load have to be computed for several interesting flight configurations

- A simple aerodynamic study has to be done to know the aerodynamic proprieties of the aircraft

- Eventually, all of the previous parts can be used to create a finite element model of the plane in the flight configuration selected.

The results found with the final finite element model will allow us to approve the structure used or suggest some modifications to improve it.

The first step of the analysis consists in performing a three-point bending test with samples of the composite material. Then the test is simulated in Samcef which is a software which implements a final element method solver. The correlation of the experimental tests and the finite element model allows to conclude that the proprieties of the material provided by the manufacturer are correct and represent the real behavior of the material.

The second step is the development of a finite element model of the whole aircraft. The validity of the model is verified by performing an experimental bending test of the drone. The displacements from the model and the real tests are compared. The results show that the model is a bit more stiff than the real aircraft which was an expected result and this allow to validate the results of the finite element model.

The last step consists in simulating a real flight configuration when the plane undergoes high aerodynamic loads. The situation selected is a resource which consists in a dive of the plane followed by a recovery. The aerodynamic loads are computed in PanAir and are imported on the finite element model. The results show that the structure is able to resist to those loads and a possible optimization of the material is proposed as some elements presents some stresses far from their yield strength.

Chapter 2

Study of the material

Before studying the behavior of the whole drone, it is necessary to know as well as possible the material that is used.

The study of the material is done in a few steps. First of all, bibliographic researches is done to find the maximum amount of data in order to build the most accurate finite element model on Samcef Field. Then the design of a sample is built on Samcef and the simulations of a three-point bending test are performed to have a great overview of the behavior of the material. The relevant results from the finite element model makes us able to prepare the experimental testing. Eventually, the results are compared and allow us to validate the proprieties of the material.

2.1   Working with composite

The drone is manufactured by Refitech which is a society based in Breda (Nederlands). They are specialized in the manufacture of carbon fiber composite products such as car's ailerons and tube profiles. The material they selected for the skin of the drone is a T700S carbon fiber composite produced by Torayca in France. The T700S is characterized by a high tensile strength while being really cost efficient which is a good compromise for the Guardian Eye as it reduces the cost of manufacturing. It has been used for more then 30 years in a many different areas which makes the documentation about its mechanical proprieties huge. They chose to use 4 plies of twilled carbon fiber, every plies are oriented in the same direction. The sheets of the composite material are prepreg which means that the carbon fibers are already included in the resin matrix before the molding.

Each ply comes from a sheet of 200 g/m^2 which corresponds to a thickness of 0.13mm according to the website of Torayca. From this data, the density of the material can be computed:

$$\rho = \frac{SurfacicWeight}{Thickness} = \frac{0.2}{0.13 * 10^{-3}} = 1.53 * 10^3 kg/m^3 \tag{2.1}$$

As the drone is made of carbon fiber composite, the pretty simple laws of isotropic material are no longer relevant. The material is anisotropic and other theories must be used.
In the literature, the proprieties of the composite material are usually presented for a unidirectional ply. It means that all of the fibers are directed in the same direction, an example is shown

at figure 2.1. Before studying it in details, we can already understand that the unidirectional material will have some strong mechanical proprieties along the axis parallel to the fibers (X-axis) as the fiber are used to reinforce the material and some weaker proprieties along the axis transverse to the fibers (Y or Z-axis). As a single ply is considered for now, all the data can be separated in two groups, the data along the X-axis and the data along the axis orthogonal to it. For a single ply, the proprieties along the Y-axis are the same then the proprieties along the Z-axis. This explains why the manufacturer usually gives the data along two axis. The proprieties for a more complex laminated composite can be computed afterward by the user.
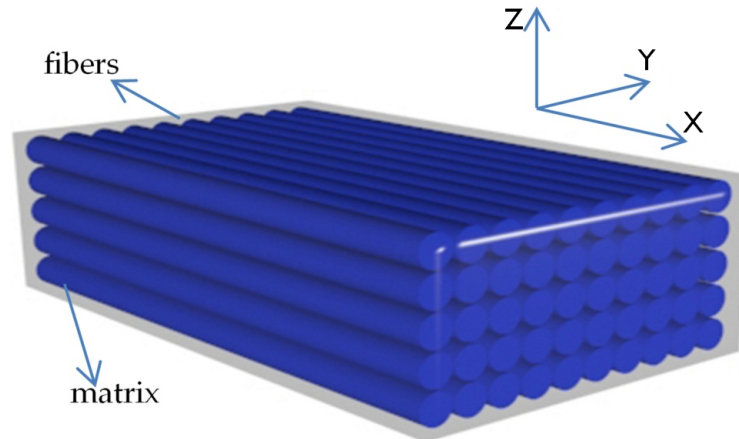
Figure 2.1: Unidirectional composite example

The proprieties needed can be introduced. The 2D linear elastic law which links the stresses to the strains for an orthotropic material can be written as:

$$\begin{pmatrix} \epsilon_{xx} \\ \epsilon_{yy} \\ \epsilon_{xy} \end{pmatrix} = \begin{pmatrix} \frac{1}{E_x} & -\frac{\nu_{yx}}{E_y} & 0 \\ -\frac{\nu_{xy}}{E_x} & \frac{1}{E_y} & 0 \\ 0 & 0 & \frac{1}{2\mu_{xy}} \end{pmatrix} \begin{pmatrix} \sigma_{xx} \\ \sigma_{yy} \\ \sigma_{xy} \end{pmatrix} \tag{2.2}$$

In this equation, ϵ is the strain, σ is the stress, E_i is the Young's modulus along a given axis, ν_{xy} and ν_{yx} are the major and minor Poisson ratios. The Poisson ratio express the contraction of a material perpendicularly to an applied tension. Eventually, μ_{xy} is the shear modulus. The matrix which is linking the strains to the stress is the material elasticity tensor and it has to be define positive.

As expected, the finite element software needs those values to perform a test.
The data provided by the manufacturer are shown in the table below:

Axis	X	Y
Young's Modulus	125e3 MPa	13e3 MPa
Plane	XY	YX
Shear Modulus	4.4e3 MPa	/
Poisson ratio	0.28	/

Figure 2.2: Data provided by the manufacturer

It contains the main parameters but it is still incomplete as some of proprieties are hard to determine. For example, the Poisson ratios and the shear modulus are not provided in certain planes. Some researches in the literature have been done (see source [9][10][11]) and they all seem to agree on the value of the missing proprieties close to a 10 percent margin. Also, an interesting article has been written by the University of Transilvania ([9]) for the same material that is used and the paper with all of the tests performed is available. The values provided in this article will be used to complete our set of data. Note that this set of data is not complete yet and will be completed in the next section with proprieties such as the tensile strength and the shear strength.

When inserting such parameters in Samcef, we can notice that all of the parameters are not necessary. For example, only the value of the major Poisson ratio (ν_{xy}) is asked while the value of ν_{yx} isn't. It is actually calculated by the software thanks to a compatibility equation. The values of both Poisson ratio can be calculated theoretically from the proprieties of the matrix and the fibers.
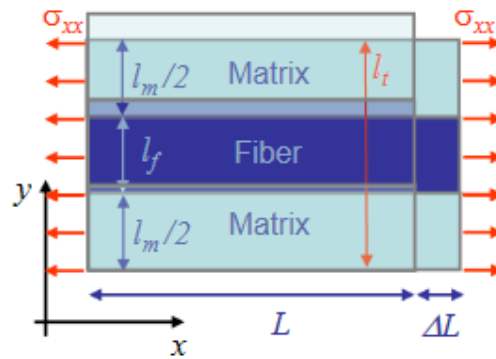
Figure 2.3: Schema of a unidirectional composite material undergoing a tensile stress in the fiber direction

By considering a single ply of a composite material with the fiber directed along the X-axis (see figure 2.3), a matrix volume ratio of v_m and a fiber volume ratio of v_f, a constrain along the X-axis will results in a small displacement ΔL, we know that the transverse displacement along the Y-axis will be:

$$\Delta l_t = \Delta l_f + \Delta l_m \tag{2.3}$$

By taking a look at the fibers and the matrix apart, we know from the linear elasticity theory that:

$$\Delta l_f = -\nu_f \epsilon_{xxf} l_f = -\nu_f l_f \epsilon_{xxtotal}, \Delta l_m = -\nu_m \epsilon_{xxm} l_m = -\nu_m l_m \epsilon_{xxtotal} \tag{2.4}$$

The resultant strain can be computed as:

$$\Delta l_t = -\nu_{xy} \epsilon_{xx} l_t \tag{2.5}$$

Injecting this result in the equation 3.3, we find:

$$-\nu_{xy} \epsilon_{xx} l_t = \Delta l_t = \Delta l_f + \Delta l_m = -\nu_f \epsilon_{xx} l_f - \nu_m \epsilon_{xx} l_m \tag{2.6}$$

$$\Rightarrow \nu_{xy} = \nu_f \frac{l_f}{l_t} + \nu_f \frac{l_m}{l_t} = \nu_f v_f + \nu_m v_m \tag{2.7}$$

Now, we can make the same reasoning for a constrain along the Y axis, we have the configuration shown at figure 2.4.
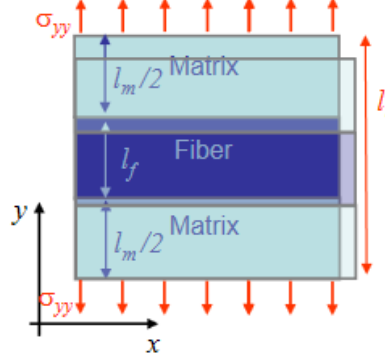
Figure 2.4: Schema of a unidirectional composite material undergoing a tensile stress perpendiculary to the direction of the fibers

We know that the strain along the X-axis will be:

$$\epsilon_{xx} = \frac{\Delta L}{L} = -\nu_{yx}\epsilon_{yy} = \nu_{yx}\frac{\sigma_{yy}}{E_y} \tag{2.8}$$

Again, if we take a look at the strain of the fibers and the matrix apart, we find the compatibility equations :

$$\epsilon_{xxf} = \frac{1}{E_f}(\sigma_{xxf} - v_f\sigma_{yyf}) = \frac{1}{E_f}(\sigma_{xxf} - v_f\sigma_{yy}) \tag{2.9}$$

$$\epsilon_{xxm} = \frac{1}{E_m}(\sigma_{xxm} - v_f\sigma_{yym}) = \frac{1}{E_m}(\sigma_{xxm} - v_m\sigma_{yy}) \tag{2.10}$$

As the resultant stress along the X-axis must be equal to 0, we have:

$$\sigma_{xxf}l_f + \sigma_{xxm}l_m = 0 \Rightarrow \sigma_{xxf}l_f = -\sigma_{xxm}l_m \tag{2.11}$$

Injecting this result in the compatibility equation:

$$\frac{1}{E_f}(-\frac{v_m}{v_f}\sigma_{xm} - \nu_f\sigma_{yy}) = \frac{1}{E_m}(\sigma_{xxm} - v_m\sigma_{yy}) = -\nu_{yx}\frac{\sigma_{yy}}{E_y} \tag{2.12}$$

The equality on the right can be used to find a relation between σ_{xxm} and σ_{yy} and then the equality on the left is used to get rid of every σ and leads to the expression:

$$\nu_{yx} = \nu_{xy}\frac{E_y}{E_x} \tag{2.13}$$

This relation between ν_{xy} and ν_{yx} is used by Samcef to find the value of ν_{yx}. The same reasoning can be done in 3D and leads to : $\frac{\nu_{xy}}{E_x} = \frac{\nu_{yx}}{E_y}$, $\frac{\nu_{xz}}{E_x} = \frac{\nu_{zx}}{E_z}$ and $\frac{\nu_{yz}}{E_y} = \frac{\nu_{yz}}{E_y}$,

A few remarks can be done, as the Young's modulus is higher along the direction of the fiber, it means that the material is stiffer along this axis. The Poisson ratio are also interesting, the major Poisson ratio (ν_{xy}) is higher than the minor one as $E_x > E_y$. In practice, we can understand it like that: If we apply a deformation along the X-axis, the deformation induced along the Y or Z-axis will be high as the material is pretty soft perpendicularly to the fiber, it leads to a big Poisson ratio. In the opposite case when a deformation is applied along the Y-axis, the deformation induced along the X-axis will be tiny has the Young's modulus in the fiber direction is really high which makes the material very stiff in this direction and the minor Poisson ratio is small.

The data used for now are summarized in the table below:

Thickness of the plies	0.13 mm	/	/
Mass Density	1530 kg/m^3	/	/
Axis	X	Y	Z
Young's Modulus	125e3 MPa	13e3 MPa	13e3 MPa
Plane	XY	XZ	YZ
Shear Modulus	4.4e3 MPa	4.4e3 MPa	3.2e3 MPa
Poisson ratio	0.28	0.28	0.07

Figure 2.5: Summary of all the proprieties of the composite material

The proprieties for a single ply is now known but the material used by Refitech is a twilled carbon fiber composite and four layers are used everywhere on the aircraft. The data for a single unidirectional ply can be used to model the configuration used on the aircraft. The composite material will be considered as a shell element in the Finite element software. This hypothesis allows to make the development done by Mr Noels in his composite idealization course[5]. It consists in the following development:

The linear elasticity law in 3D can be written as $\sigma_{ij} = C_{ijkl}\epsilon_{kl}$ or under the matrix form:

$$
\begin{pmatrix} \sigma_{xx} \\ \sigma_{yy} \\ \sigma_{zz} \\ \sigma_{yz} \\ \sigma_{zx} \\ \sigma_{xy} \end{pmatrix} = \begin{pmatrix} C_{xxxx} & C_{xxyy} & C_{xxzz} & 0 & 0 & 0 \\ C_{yyzz} & C_{yyyy} & C_{yyzz} & 0 & 0 & 0 \\ C_{zzxx} & C_{zzyy} & C_{zzzz} & 0 & 0 & 0 \\ 0 & 0 & 0 & 2C_{yzyz} & 0 & 0 \\ 0 & 0 & 0 & 0 & 2C_{xzxz} & 0 \\ 0 & 0 & 0 & 0 & 0 & 2C_{xyxy} \end{pmatrix} \begin{pmatrix} \epsilon_{xx} \\ \epsilon_{yy} \\ \epsilon_{zz} \\ \epsilon_{yz} \\ \epsilon_{zx} \\ \epsilon_{xy} \end{pmatrix} \tag{2.14}
$$

The matrix has this form because if we look at the stress σ_{yz} for example, we have:

$$
\sigma_{yz} = C_{yzkl}\epsilon_{kl} = C_{yzyz}\epsilon_{yz} + C_{yzzy}\epsilon_{zy} = 2C_{yzyz}\epsilon_{yz} \tag{2.15}
$$

The reasoning can be done for σ_{zx} ans σ_{xy} resulting in the equation 2.14. The different C_ijkl are given by:

$$C_{xxxx} = \frac{1 - \nu_{yz}\nu_{zy}}{E_y E_z D}, C_{xxyy} = \frac{\nu_{yx} + \nu_{zx}\nu_{yz}}{E_y E_z D}, C_{xxxx} = \frac{\nu_{zx} + \nu_{yx}\nu_{zy}}{E_y E_z D} \tag{2.16}$$

$$C_{yyxx} = \frac{\nu_{xy} + \nu_{zy}\nu_{xz}}{E_x E_z D}, C_{yyyy} = \frac{1 - \nu_{xz}\nu_{zx}}{E_x E_z D}, C_{xxxx} = \frac{\nu_{zy} - \nu_{xy}\nu_{zx}}{E_x E_z D} \tag{2.17}$$

$$C_{zzxx} = \frac{\nu_{xz} - \nu_{xy}\nu_{yz}}{E_y E_x D}, C_{zzyy} = \frac{\nu_{yz} - \nu_{xz}\nu_{yx}}{E_y E_x D}, C_{zzzz} = \frac{1 - \nu_{yx}\nu_{xy}}{E_y E_x D} \tag{2.18}$$

$$C_{yzyz} = C_{yzzy} = C_{zyzy} = C_{zyyz} = \mu_{yz} \tag{2.19}$$

$$C_{xyxy} = C_{xyyx} = C_{yxyx} = C_{yxxy} = \mu_{xy} \tag{2.20}$$

$$C_{xzxz} = C_{xzzx} = C_{zxzx} = C_{zxxz} = \mu_{xz} \tag{2.21}$$

$$D = \frac{1 - \nu_{xy}\nu_{yx} - \nu_{yz}\nu_{zy} - \nu_{xz}\nu_{zx} - 2\nu_{xy}\nu_{yz}\nu_{zx}}{E_x E_y E_z} \tag{2.22}$$
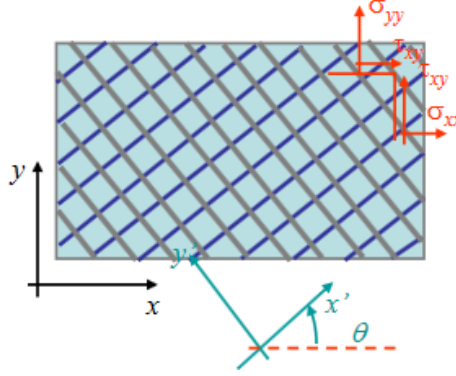
Figure 2.6: Case of an ply with an orientation θ

For a plane stress state and a ply oriented with an angle θ compared to the main X-axis (see figure 2.6), in the system of axis O'x'y', we have:

$$\begin{pmatrix} \sigma_{x'x'} \\ \sigma_{y'y'} \\ \sigma_{x'y'} \end{pmatrix} = \begin{pmatrix} \frac{E_{x'}}{1-\nu_{x'y'}\nu_{y'x'}} & \frac{\nu_{y'x'}E_{x'}}{1-\nu_{x'y'}\nu_{y'x'}} & 0 \\ \frac{\nu_{y'x'}E_{y'}}{1-\nu_{x'y'}\nu_{y'x'}} & \frac{E_{y'}}{1-\nu_{x'y'}\nu_{y'x'}} & 0 \\ 0 & 0 & 2\mu_{x'y'} \end{pmatrix} \begin{pmatrix} \epsilon x'x' \\ \epsilon_{y'y'} \\ \epsilon_{x'y'} \end{pmatrix} \tag{2.23}$$

This can be expressed under the tensor form: $\boldsymbol{\sigma'} = \mathbf{C} : \boldsymbol{\epsilon'}$. As θ is the angle between the system of axis, we have: $\boldsymbol{\sigma'} = \mathbf{R} \, \boldsymbol{\sigma} \mathbf{R}^T$ and $\boldsymbol{\epsilon'} = \mathbf{R} \, \boldsymbol{\epsilon} \mathbf{R}^T$. With $\mathbf{R}$ being the matrix of rotation. The expression needed is of the form $\boldsymbol{\sigma} = \mathbf{C} : \boldsymbol{\epsilon}$. The solution is:

$$\mathbf{R} \, \sigma \mathbf{R}^T = C' : \mathbf{R}\epsilon\mathbf{R}^T \tag{2.24}$$

$$\Rightarrow \sigma_{ij} = R_{ki}C'_{klmn}R_{lj}R_{mp}\epsilon_{pq}R_{nq} = R_{ki}R_{lj}C'_{klmn}R_{mp}R_{nq}\epsilon_{pq} = C_{ijpq}\epsilon_{pq} \tag{2.25}$$

Which is the expression we were looking for. This can be applied to all the C_{ijkl} needed to find the proprieties of the ply in the system of axis Oxy. The ply can be assembled after ward. The linear elasticity law in a plane stress state can be written under the form:

$$\begin{pmatrix} \sigma_{xx} \\ \sigma_{yy} \\ \sigma_{xy} \end{pmatrix} = \frac{1}{h} \begin{pmatrix} A_{xxxx} & A_{xxyy} & 2A_{xxxy} \\ A_{yyxx} & A_{yyyy} & 2A_{yyxy} \\ A_{xyxx} & A_{xyyy} & 2A_{xyxy} \end{pmatrix} \begin{pmatrix} \epsilon_{xx} \\ \epsilon_{yy} \\ \epsilon_{xy} \end{pmatrix} \quad (2.26)$$

Where $A^i_{abcd} = \sum_i t_i C^i_{ijkl}$ with t_i being the the thickness of the ply and h the thickness of the laminated composite. The method can be resumed like that: The parameters (element of the matrix C'_{ijkl}) of each plies are expressed in the system of axis Oxy then all of the element C^i_{ijkl} are weighted in function of their thickness and are added together to find the proprieties of the whole laminated composite.

This method allows to model the superposition of layers of our choice in Samcef. In our case, it is needed to model four plies of twilled carbon fiber composite and each of the ply has a thickness of 0.13 mm. The last problem needed to be solved is the modeling of the twilled layers. In order to model a twilled ply of 0.13 mm, the best method is to create two plies of 0.065 mm perpendicular to each other. The final configuration of our composite material is shown at figure 2.7.
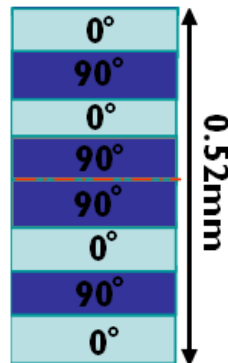
Figure 2.7: Configuration of the laminated composite

In this configuration, we can notice that the orientation of the plies is symmetrical about the neutral fiber. This is done is order to remove the tensile/shearing coupling in the composite.

2.2 Failure criteria

In order to know if the material is close to its limit of elasticity, it is not possible to rely on the von Mises criteria as this is only valid for an isotropic material. The Tsai-Hill criterion has to be introduced.

The von Mises criterion is used as a basis and an analogy is made to find a criterion for orthotropic materials. The von Mises criterion tells that the limit of elasticity of an isotropic material is reached when:

$$\frac{1}{2}[(\sigma_{11} - \sigma_{22})^2 + (\sigma_{22} - \sigma_{33})^2 + (\sigma_{33} - \sigma_{11})^2 + 6(\sigma_{23}^2 + \sigma_{31}^2 + \sigma_{12}^2)] = \sigma_y \qquad (2.27)$$

Where σ_y is the yield strength of the material.

By taking this expression, it can be assumed that failure of an orthotropic material will occur when the same kind inequality is not verified anymore:

$$a(\sigma_{LL} - \sigma_{TT})^2 + b(\sigma_{TT} - \sigma_{ZZ})^2 + c(\sigma_{ZZ} - \sigma_{LL})^2 + d\sigma_{LZ}^2 + e\sigma_{TZ}^2 + f\sigma_{LT}^2 < 1 \qquad (2.28)$$

Note that the general form of the equation is the same than the von Mises one except that it introduces some coefficients (a, b, c,...) that are used to take the anisotropy of the material into account. This equation is written in the system of axis L-T-Z attached to the material. L is the axis parallel to the fiber direction, Z is the axis along the thickness of the ply and T is the axis orthogonal to L and T, transverse to the fiber direction.

By considering a stress only along the L axis ($\sigma_{TT} = \sigma_{ZZ} = \sigma_{LZ} = \sigma_{TZ} = \sigma_{LT} = 0$), we find that the inequality is not verified any more for a certain value of (a+c). We set this value to $a + c = 1/\sigma_{Lu}^2$, by doing the same along the other axis ($a + b = 1/\sigma_{Tu}^2$ and $b + c = 1/\sigma_{Zu}^2$) and then considering the case of a plane stresses (L,T), all the constants are found and eventually gives the inequality:

$$(\frac{\sigma_L}{\sigma_{Ly}})^2 + (\frac{\sigma_T}{\sigma_{Ty}})^2 - \frac{\sigma_L\sigma_T}{\sigma_{Ly}\sigma_{Ly}} + (\frac{\tau_{LT}}{\tau_{LTy}})^2 < 1 \qquad (2.29)$$

This is the Tsai-Hill criterion and this is what is used by Samcef to verify if failure occurs in an orthotropic materials.

It involves a few more variables: σ_{Ly}, σ_{Ty}, σ_{Zy}, τ_{LTy}, τ_{TZy} and τ_{LZy} which are the ultimate tensile strength and the ultimate shear strength along the different axis. All of those parameters are given by the manufacturer and are shown at figure 2.8 and they are used in the finite element software.

Axis	X	Y	Z
Tensile strength [MPa]	2.55e3	69	69
Plane	XY	XZ	YZ
Shear strength [MPa]	98	98	10

Figure 2.8: Tensile strength and shear strength of the composite material studied

2.3 Mode of failure

A typical stress-strain curve of a composite material is shown at figure 2.9. It can be seen that the behavior of the material in the zone I is linear, until the stress reaches the limit value

σ_y, the behavior becomes non linear and the theory used in this project doesn't explain this phenomenon. When the stress-strain curve becomes non linear, permanent deformation usually appear, the material is hardening and a more complex theory has to be used. When the stress reaches the limit value which is the ultimate strength, the material is necking, the section area is decreasing, large deformation occurs until the fracture of the material. The shape of the graph might seem strange has after the ultimate strength, the deformations are increasing while the stress is diminishing. It is actually explain by the definition of the stress. The stress σ used is the engineer stress and is defined as the force divided by the initial section area: $\sigma = F/S_i$ while the true stress is equal to the force divided by the effective area.
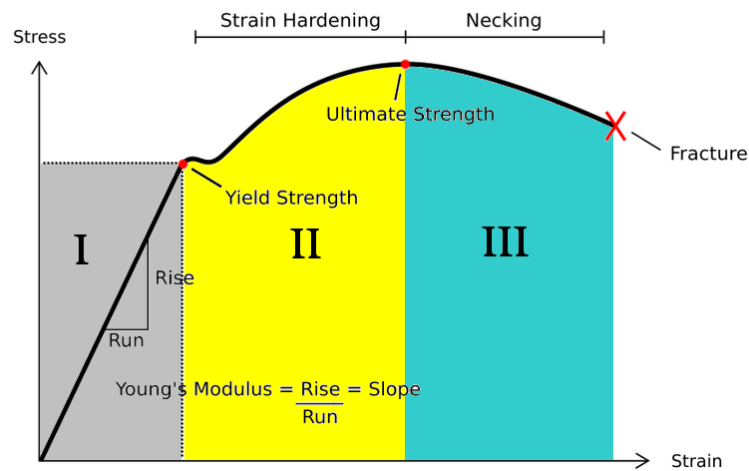
Figure 2.9: Example of a stress-strain diagram

As the linear elastic theory only explains the behavior until the yield strength, our analysis makes sens as long as the Tsai-Hill value is smaller than 1.

The non linear behavior are not studied in the report but the different modes of failure of the composite can be introduced to understand what can be dangerous for the drone if some stresses become too high.

-The fibers can simply break
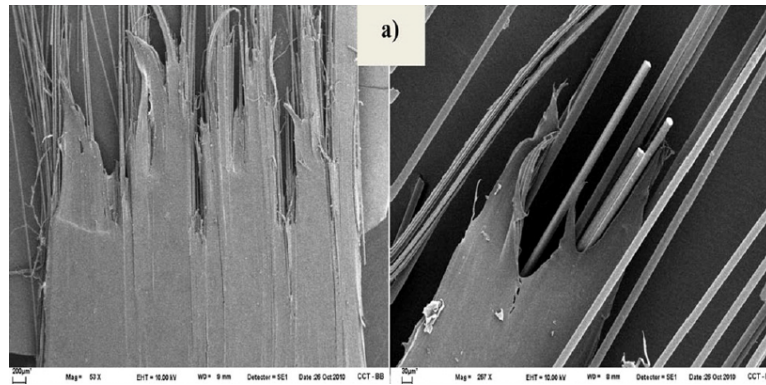
Figure 2.10: Example of a the broken fibers

-Microcracking can occur in the matrix
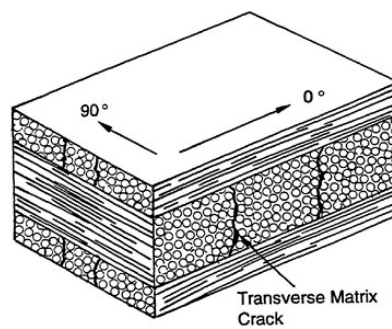
Figure 2.11: Example of a microcracking in the matrix

-The interface between the matrix and the fiber can break, this is called debonding and this is often due to a bad adhesion between the matrix and the fiber. To avoid this, fibers can be treated before being placed in the matrix.
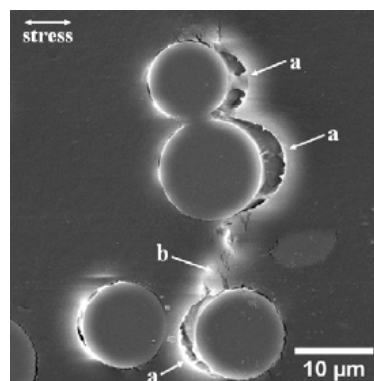
Figure 2.12: Example of a debonding of a composite

-The interface between the different layers of the composite can break which is called delamination. This phenomenon can occur for example when a composite sheet is cut. Some precaution will be taken later when cutting the samples to avoid it.
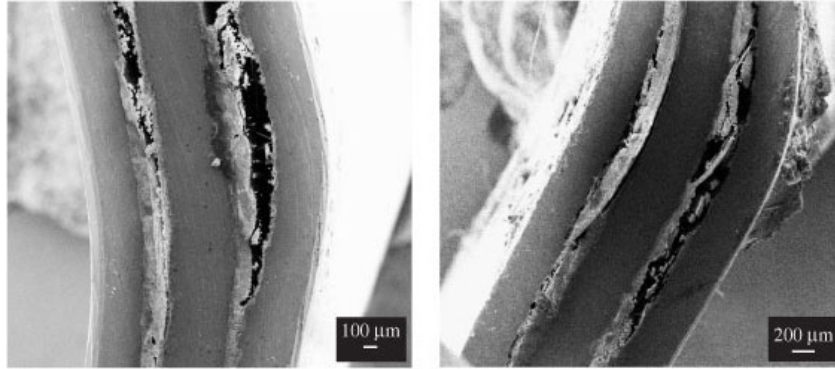
Figure 2.13: Example of a delamination of a composite

Composite materials can also be contaminated by moisture. The usage in wet conditions can lead to failure because of moisture which can diminish the mechanical proprieties of the material. However, as our aircraft is a drone, its usage time should be way shorter then the one of the airliners and it shouldn't be subject to such a phenomenon.

A last problem which is common with composite materials is their resistance to shock. They have a tendency to tear apart. Pilots often takes the example of an impact with a bird, if the skin is made of aluminum, the impact might deform the wing. If the impact occurs with a composite skin, the wing may tear apart which is much more problematic. As our drone is small and shouldn't fly faster then 100 km/h, those kind of event are very rare and less dangerous than for airliners.

2.4 Summary of the proprieties of the material

The data used are shown in the following table. The values in bold were not given by the manufacturer and were found in the literature.

Thickness of the plies	0.13mm		
Mass Density	1300 kg/m^3		
Axis	X	Y	Z
Young's Modulus	125e3 MPa	13e3 MPa	13e3 MPa
Shear Modulus	4.4e3 MPa	4.4e3 MPa	**3.2e3** MPa
Tensile Strength	2.55e3 MPa	69 MPa	69 MPa
Plane	XY	XZ	YZ
Shear Strength	98 MPa	98 MPa	**10** MPa
Poisson ratio	0.28	0.28	**0.07**

Figure 2.14: Summary of the proprieties of the composite material

A comparison with a well-known material can be done to have a good idea of the order of magnitude of those values. For example, aluminum alloys has been used for a long time in aeronautics, its Young's Modulus is about 70 GPa which is twice smaller than the Young's modulus of the T700S in the direction of the fibers. However, the proprieties of the unidirectional T700S in the Y and Z axis are weaker, this problem is solved by using laminated composite with different ply orientations. The tensile strength of the aluminum alloys is usually about 240 MPa while the tensile strength along the direction of the fiber is about 2.5 GPa, this is 10 times higher ! Eventually, the density of the composite used is about 1500 kg/m^3 while the density of an aluminum alloy is about $2700 kg/m^3$.

The low density and the high tensile strength makes the carbon fiber composite a very good choice of material for aeronautics.

2.5 Finite element model of the experimental tests of the samples

Now that all the proprieties are known, the finite element model can be built to prepare the experimental tests.

2.5.1 Introduction to Samcef

The finite element software which is used in this thesis is Samcef. Samcef is a powerful software which has been originally developed by the University of Liege and which is commercialized by Samtech. During this whole project, the linear analysis module is used because it provides great solutions with a minimum of process resources.

An introduction to the method used by the software is needed to be able to analyze the results in a proper way. It is important to underline that this section is only an introduction, some more complicated way to solve the problem can be used but a whole paper could be written about the methods used. This introduction is just done to understand the physical principle and the assumptions which are used in the method. To simplify the problem, we consider an isotropic material here but the method can be adapted to orthotropic materials too. The way the finite element method is introduced has been inspired by the course of Finite element method of Pr. Nikishkov from the University of Aizu in Japan[3].

The first step in the finite element method is to discretize the continuum structure. This is done by meshing the structure, the better mesh we are using, the better the results will be. Using a very detailed mesh will increase to size of the problem and will require more resources. A compromise as to be done to find a mesh which gives great results and not leading to a problem too complicated to solve. For this reason, a convergence analysis is usually done. In our case, the convergence of the mesh is done by looking for the convergence of the potential energy of the system.

Let's consider one node of the mesh which is associated to a nodal displacement $\mathbf{u}$:

$$\mathbf{u} = (u, v, w) \tag{2.30}$$

in the system of axis Oxyz.

The strain can be placed in a vector $\boldsymbol{\epsilon}$:

$$\boldsymbol{\epsilon} = (\epsilon_{xx}, \epsilon_{yy}, \epsilon_{zz}, \gamma_{xy}, \gamma_{yz}, \gamma_{xz}) \tag{2.31}$$

If we make the assumption of small displacement, the strain can be expressed in function of the displacement such as $\epsilon_{ij} = \frac{\delta u_i}{\delta x_j}$. This can be written under the matrix form: $\boldsymbol{\epsilon} = \mathbf{Du}$

Where $\mathbf{D}$ is the matrix of differentiation given by:

$$\mathbf{D} = \begin{pmatrix} \delta/\delta_x & 0 & 0 \\ 0 & \delta/\delta_y & 0 \\ 0 & 0 & \delta/\delta_z \\ \delta/\delta_y & \delta/\delta_x & 0 \\ 0 & \delta/\delta_z & \delta/\delta_y \\ \delta/\delta_z & 0 & \delta/\delta_x \end{pmatrix} \tag{2.32}$$

The stress associated to the node can be express with the tensor $\boldsymbol{\sigma}$:

$$\boldsymbol{\sigma} = (\sigma_{xx}, \sigma_{yy}, \sigma_{zz}, \tau_{xy}, \tau_{yz}, \tau_{xz}) \tag{2.33}$$

By using the linear elasticity law, we can relate the constrain to the stress such as :

$$\boldsymbol{\sigma} = \mathbf{H}\boldsymbol{\epsilon} \tag{2.34}$$

Where $\mathbf{H}$ is the elasticity matrix and is given by :

$$\mathbf{H} = \begin{pmatrix} \lambda + 2\mu & \lambda & \lambda & 0 & 0 & 0 \\ \lambda & \lambda + 2\mu & \lambda & 0 & 0 & 0 \\ \lambda & \lambda & \lambda + 2\mu & 0 & 0 & 0 \\ 0 & 0 & 0 & \mu & 0 & 0 \\ 0 & 0 & 0 & 0 & \mu & 0 \\ 0 & 0 & 0 & 0 & 0 & \mu \end{pmatrix} \tag{2.35}$$

Where λ and μ are function of the Young's modulus and the Poisson ratio:

$$\lambda = \frac{\nu E}{(1+\nu)(1-2\nu)}, \mu = \frac{E}{2(1+\nu)} \tag{2.36}$$

The finite element method have to find the strain field such as the potential energy of the system is minimized. The potential energy can be expressed as:

$$U_p = \int_V \frac{1}{2}\boldsymbol{\epsilon}^T \boldsymbol{\sigma} dV - \int_V \mathbf{u}^T \mathbf{p}^V \mathrm{d}V - \int_S \mathbf{u}^T \mathbf{p}^S dS \tag{2.37}$$

Where $\mathbf{p}_V$ is the vector containing the body forces and $\mathbf{p}^S$ contains the surface forces.

By applying this reasoning on an element, we can consider a vector containing the nodal displacements of all the nodes $\mathbf{q}$.

The displacements of a point inside an element can be expressed as a linear combination of the displacement of the nodes:

$$\mathbf{u} = \sum N_i u_i, v \sum N_i v_i, w = \sum N_i w_i \tag{2.38}$$

This relation can be expressed under the matrix form $\mathbf{u} = \mathbf{Nq}$ where $\mathbf{N}$ is the shape matrix made of the shape functions N_i:

$$\mathbf{N} = \begin{pmatrix} N_1 & 0 & 0 & N_2 & 0 & 0 & ... \\ 0 & N_1 & 0 & 0 & N_2 & 0 & ... \\ 0 & 0 & N_1 & 0 & 0 & N_2 & ... \end{pmatrix} \tag{2.39}$$

This allows to write the strain as a function of the shape matrix and the displacements: $\boldsymbol{\epsilon} = \mathbf{Bq}$ where $\mathbf{B} = [\mathbf{B}_1, \mathbf{B}_2, \mathbf{B}_3, ...]$ is the made of the differentiation of the shape function matrices which is the the differentiation matrix multiplied by the shape function matrices :

$$\mathbf{B}_i = \begin{pmatrix} \delta N_i/\delta_x & 0 & 0 \\ 0 & \delta N_i/\delta_y & 0 \\ 0 & 0 & \delta N_i/\delta_z \\ \delta N_i/\delta_y & \delta N_i/\delta_x & 0 \\ 0 & \delta N_i/\delta_z & \delta N_i/\delta_y \\ \delta N_i/\delta_z & 0 & \delta N_i/\delta_x \end{pmatrix} \tag{2.40}$$

By using this expression in the potential energy function, we find:

$$U_p = \int_V \frac{1}{2}(\mathbf{Bq})^T \mathbf{EBq} dV - \int_V (\mathbf{Nq})^T \mathbf{p}^V \mathrm{d}V - \int_S (\mathbf{Nq})^T \mathbf{p}^S dS \tag{2.41}$$

The minimum of this function is found by finding the 0 of its derivatives and we end up with:

$$\int_V \mathbf{B}^T \mathbf{EB} dV \mathbf{q} - \int_V \mathbf{N}^T \mathbf{p}^V \mathrm{d}V - \int_S \mathbf{N}^T \mathbf{p}^S dS = 0 \tag{2.42}$$

This equation can be expressed as the simple matrix equation:

$$\mathbf{Kq} = \mathbf{f} \tag{2.43}$$

Where $\mathbf{K}$ is the stiffness matrix given by $\mathbf{K} = \int_V \mathbf{B}^T \mathbf{EB} dV$ and $\mathbf{f}$ is the vector which contains all of the body and surface forces: $f = \int_V \mathbf{N}^T \mathbf{p}^V \mathrm{d}V + \int_S \mathbf{N}^T \mathbf{p}^S dS$

This is done for each finite element, which give us all of the the $\mathbf{K}_i$ and $\mathbf{f}_i$ matrices. We introduce the three matrices $\mathbf{Q}_d, \mathbf{F}_d$ and $\mathbf{K}_d$ such as:

$$\mathbf{Q}_d = [\mathbf{q}_1, \mathbf{q}_2, ...] \mathbf{F}_d = [\mathbf{f}_1, \mathbf{f}_2, ...] \mathbf{Q}_d = diag(\mathbf{K}_1, \mathbf{K}_2, ...) \tag{2.44}$$

It is possible to find a matrix of transformation $\mathbf{A}$ such as:

$$\mathbf{Q}_d = \mathbf{A}\mathbf{Q}, \mathbf{F}_d = \mathbf{A}\mathbf{F} \tag{2.45}$$

By injecting those relations in the potential energy function and after derivation, we end up with the final system which represents our structure:

$$\mathbf{A}^T\mathbf{K}_d\mathbf{A}\mathbf{Q} - \mathbf{A}^T\mathbf{F}_d = 0 \tag{2.46}$$

$$\Rightarrow \mathbf{K}_{final}\mathbf{Q} = \mathbf{F}_{final} \tag{2.47}$$

In this system of equation, the boundary conditions can be applied to remove the rigid body modes and simulate the configuration of the structure. The vector $\mathbf{Q}$ contains all of the nodal displacements and is the unknown. The software uses an algorithm to invert the matrix $\mathbf{K}_{final}$ and find the solution. As the matrix $\mathbf{K}_{final}$ has to be inverted, we can understand that it can't be singular. If a rigid body mode is still present, the matrix $\mathbf{K}$ becomes singular and impossible to invert leading to a failure of the method. For this reason, we have to make sure that all of the rigid body modes are removed in every model we will use.

2.5.2 Simulation of the experimental test

The test consists in a three-point bending test and the sample must be designed in function of the available machine. A picture of the configuration of the machine is shown at figure 2.15.
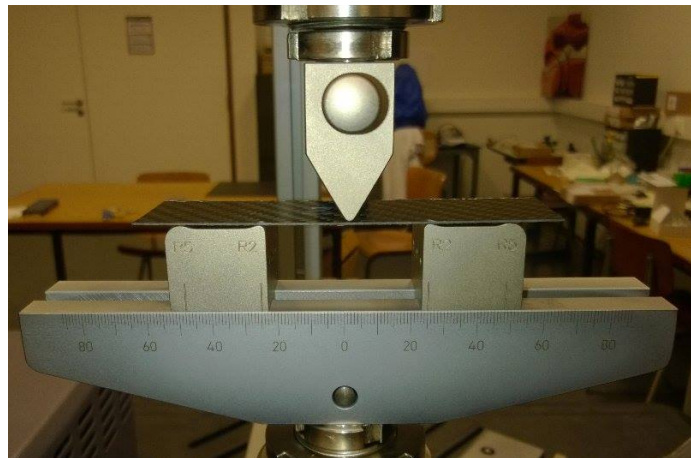
Figure 2.15: Configuration of the three-point bending test

As we can see on the picture, there is a space of about 3 cm available under the sample. Then, the maximum deflection of the sample must be lower then 3 cm. Also, the support is 3cm wide, then the width of the sample is set to 3cm. The first length chosen for the sample was 7cm as it lead to a maximum deflection of 1.5cm when the value of the Tsai-Hill was 1 on the finite element model. However, during the real test, we noticed that the failure occurred way after we reached the limit of elasticity of the Samcef model. It was noticed that the samples were not broken when the displacement of the cross head section reached 1.5cm. After this point, we observe a non linear behavior. We changed the sample in order to reach higher stresses. The distance between the supports was set to 5cm to increase the stresses caused by the displacements. This configuration also allow us to break the samples. Then, the sample to model are 5 by 3 cm.

To model the sample in Samcef, a rectangular face is created and is considered as a shell element. The proprieties of a single ply is given to the software and the configuration (the thickness and the orientation) of the plies is also encoded. The mesh of the sample is created and the convergence of the energy of the system is used to check that the mesh is good. The model is shown at figure 2.16.
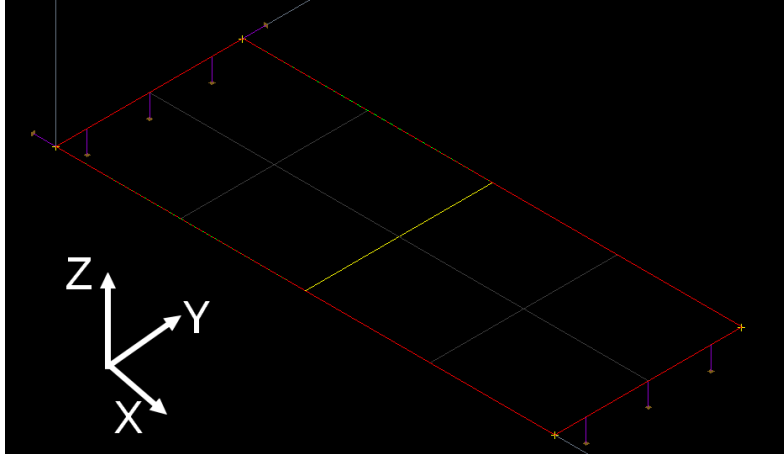
Figure 2.16: Model of the three-point bending test

Another important thing in the finite element model are the boundary conditions used. Obviously, we must lock the displacement along the Z-axis at the beginning and the end of the sample to simulate the roller supports. As explained before, we also need to remove the rigid body modes of the structure, this is made by prescribing the displacement of two points in contact with the supports along the X and Y axis.

Eventually, we can apply a line force at the middle of the sample to simulate the moving pin. As we are using a static model, we only apply a few different forces in order to plot the stress-strain curve. We don't need to test it for a lot of different forces as the behavior of the material has to be linear for a Tsai-Hill smaller than 1. For each force applied, we also check the maximum value of the Tsai-Hill criterion and finally find when the limit of elasticity is reached. The maximum cross head displacement of the sample found is 5.6mm.

Samcef allows to see the deflection in every configurations. The nodal displacement for a force of 70 N is shown at figure 2.15. As expected, the deformations are characteristic of a three-point bending test.
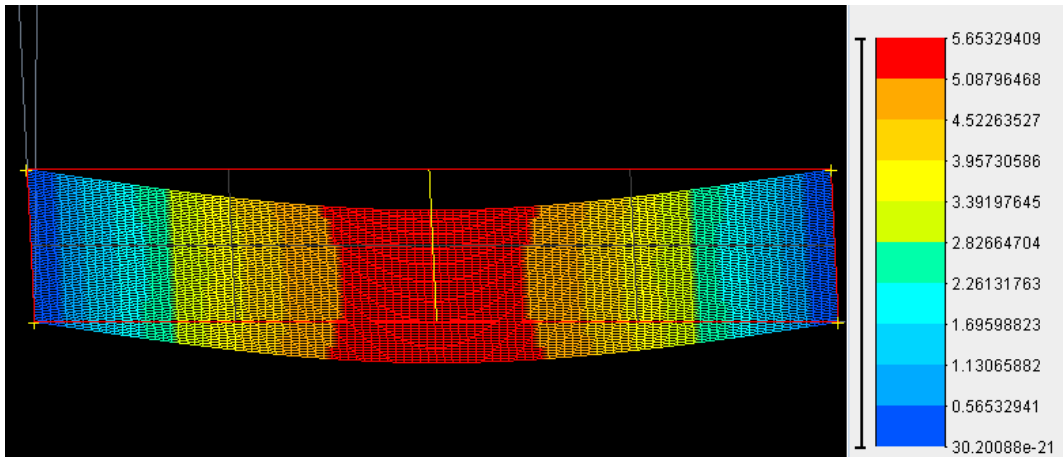
Figure 2.17: Nodal displacement for a force of 70N

The behavior of the sample is indeed perfectly linear. The model can't be used for a higher force as the linear laws used by the solver wouldn't represent the real behavior of the material for a Tsai-Hill greater then 1. From this model, the real samples should undergo a non linear behavior for a force higher than 70 N and a crosshead displacement of 5.6 mm.

Plotting the evolution of the Tsai-Hill values is also interesting:
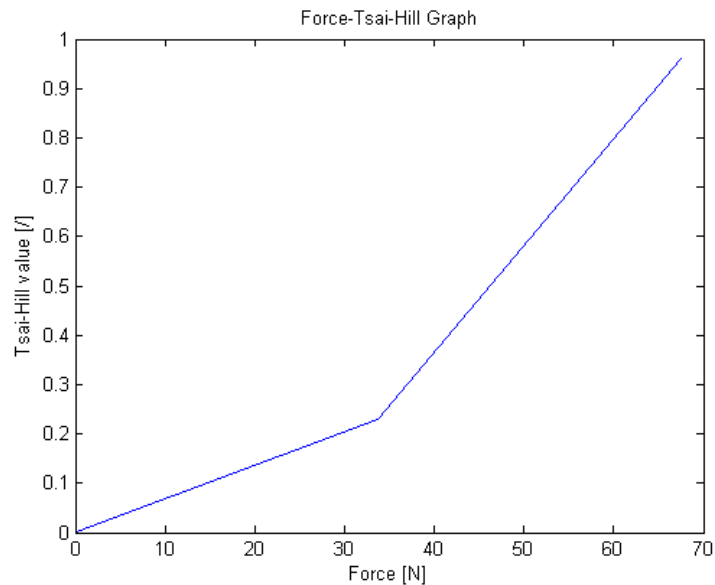
Figure 2.18: Evolution of the maximum Tsai-Hill value in function of the applied force

We can see at figure 2.18 that the relation between the Tsai-Hill value and the force applied is non linear.

We can also take a look at the distribution of the stresses. This is shown at figure 2.19. As explained before, the highest stress is reached at the middle of the sample where the load is applied. It can be noticed that the stress is even higher on the side of the sample.
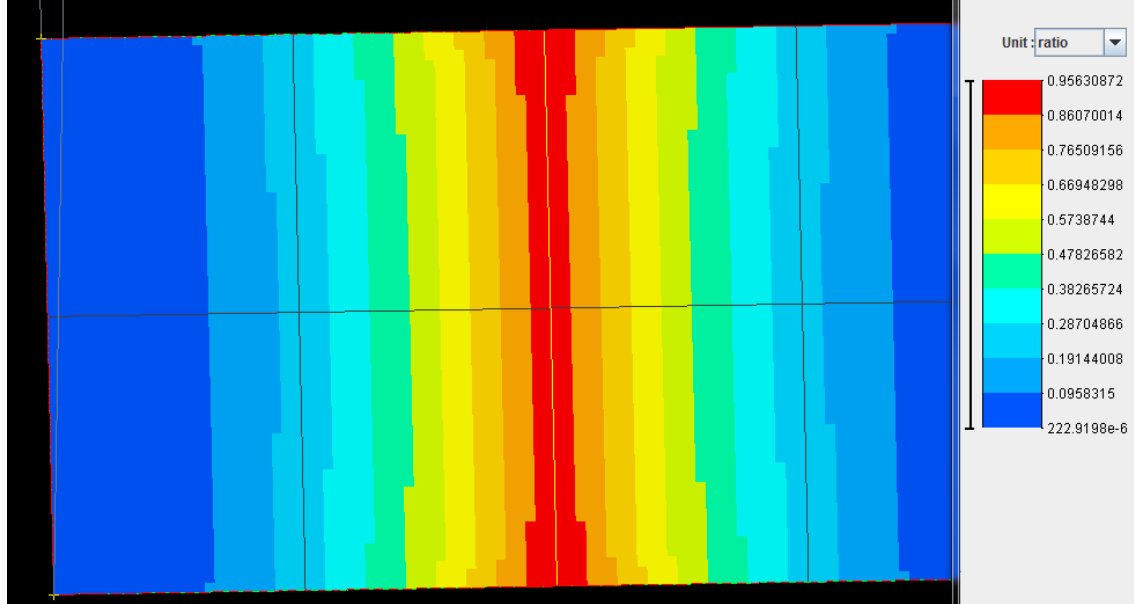
Figure 2.19: Tsai-Hill value for an applied force of 70 N

2.6 Sensitivity analysis

The sensibility of each parameters can be studied in order to know which parameters are influencing the results of the test. If a parameter doesn't influence the test, it means that the test is not adapted to measure it. The value of a series of parameters are changed for a force of 70 N.

The main parameters are changed one by one and the output parameters (the Tsai-Hill value and the cross head displacement) are checked every time. In the table below, the parameter which has been changed is written in red.

E_x[MPa]	E_{y-z}[MPa]	μ_{xy}[MPa]	σ_x^{limit}[MPa]	$\sigma_{y.z}^{limit}$[MPa]	Tsai-Hill value[/]	Max. disp.[mm]
125e3	13.3e3	4.4e3	2.55e6	69	0.95	5.6
60e3	13.3e3	4.4e3	2.55e6	69	**3.7**	**11.3**
125e3	5e3	4.4e3	2.55e6	69	**0.14**	**5.7**
125e3	13.3e3	1e3	2.55e6	69	0.95	5.6
125e3	13.3e3	4.4e3	1e6	69	0.95	5.6
125e3	13.3e3	4.4e3	2.55e6	50	**1.81**	5.6

Figure 2.20: Sensibility analysis of the parameters

The value of the Poisson ratio wasn't changed as it has almost no influence in this three-point bending test. We can notice that the Young's modulus plays a huge role in the test. If the value of E_x is lowered, the material becomes less stiff, bigger deformations occurs and the values of the Tsai-Hill increase.

Diminishing the Young's modulus E_y and E_z almost doesn't change the nodal displacement. It can be explain by the fact that the value of E_x is huge compared to E_y and E_z, the plies with the fibers oriented along the X-axis (system of axis shown at figure 2.16) try to prevent the displacement. However, the value of the Tsai-Hill is lower because the plies with the fibers oriented along the Y-axis are soft in the X-direction and can be deformed more easily without increasing the value of Tsai-Hill drastically.

The shear modulus almost have no role in the test as our samples are very thin, another test is proposed at the end of this section to check this propriety.

Eventually, the influence of the tensile strength is studied. We can notice that the value of the tensile strength along the fiber direction has almost no impact on the results while the tensile strength in the other directions have a big influence on the value of the Tsai-Hill. Of course, as expected, the tensile strength doesn't influence the nodal displacement in the model as it doesn't appear in the linear elasticity law.

This analysis allows us to conclude that all of the parameters can't be checked by this simple three-point bending tests. Some other tests could be performed to check those parameters. The shear strength and the shear modulus are usually checked by a tree-point bending test, however, in our case, as the samples are very thin, this parameter is hard to check. A tensile test could be performed with some samples with plies oriented at +/-45 degrees directions. Those samples could be cut out of the composite sheet provided. The problem in this case would be the manufacturing of the samples as cutting them with an exact angle of 45 degrees is a perilous task.

Another test could be performed to verify the value of the Poisson ratio. A simple tensile test could be done, the longitudinal displacement could be measured and another measuring machine such as a laser beam could be used to measure the transverse displacement. However, as the material has a huge module of elasticity, the displacements would be tiny and hard to calculate accurately. The second problem is that the displacements along the thickness would be impossible to measure as the sample is really thin. The best option would be to use a sample with unidirectional fiber direction and compute the displacements along the width.

Eventually, a last test which is often used to verify the proprieties of materials susceptible to micro cracking propagation is the four-point bending tests. The configuration of this test is shown at figure 2.21. The advantage of this test is that the moment between the movable pins is constant. The maximum stress is higher on larger part of the sample. If a default is present in the composite material, the sample will break for an applied force smaller. It allows to measure the limit of the material more realistically. In our case, as we are only studying the linear elastic behavior of the material, this test was not needed.
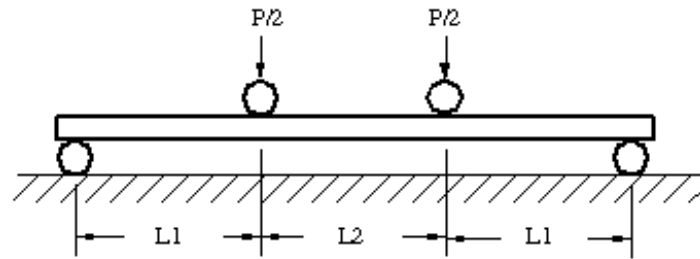
Figure 2.21: Configuration of a four-point bending test

2.7   Manufacturing of the samples

To perform the experimental tests, Refitech sent a 40 by 60 cm composite sheet that is used on the drone. First of all, the thickness of the sheet is verified and we noticed that the sheet doesn't have to same thickness every where. Indeed, the right side of the sheet is 0.52mm thick while the thickness of the left side is only 0.39 mm. The demarcation of those zones can be seen clearly on the composite sheet and it is shown at figure 2.22. It is not hard to understand that a part of the composite sheet is made of three layers while the other part is made of four layers.
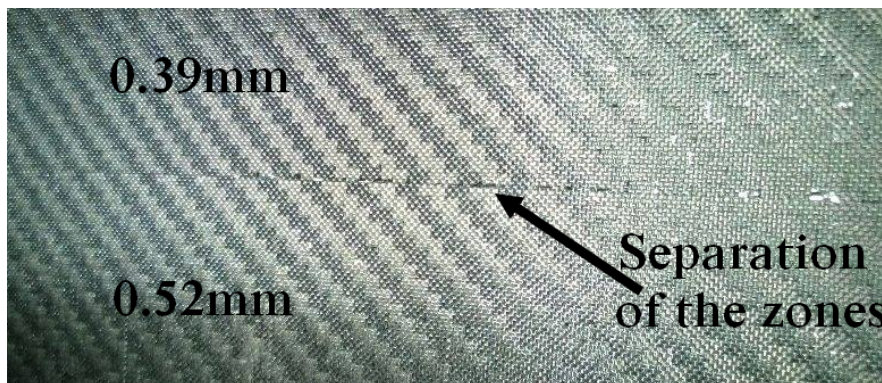
Figure 2.22: Separation of the three and four layers part of the composite sheet

The samples had to be cut out of the sheet. As the carbon fiber composite is a very hard material, the tool used to cut the sheet needs to be very hard, harder then the one used to cut steel. Moreover, cutting composite is a perilous task. We need to be sure that the damage it causes to the material are minimal. If delamination occurs, even on the side of the sample (remember from figure 2.19 that the constrains were higher on the sides), it can alter the proprieties of the material. Also, the cuts must be precise enough so that all the samples have to same size. Eventually, the cut must be done exactly in the same direction. As it has been said earlier, the orientation of the fiber influences the mechanical proprieties, then we must be sure that the direction of the fiber is the same in the finite element model and on the real samples.

The best tool to cut it would have been the water jet cutter because it would have done a sharp cut without any delamination or heating problem. Unfortunately, this kind of machine is not available at the University of Liege and an order had to be made to a company which would have cost money and a lot of time because of the delays. The second option considered was the Dremel but it was rejected has the friction between the tool and the material releases a lot of heat which could have cause damages.

The solution used to cut the samples was an angle grinder with a really hard disk and a high rotational speed. The disk used is reinforced with diamond and is the one used to cut marble and tiles.

The equipment required to cut carbon fiber composite is also important, a mask, glaces and gloves are needed because the emanation and the dust are toxic. The cut is done outside to prevent any contamination.

The part of the sheet which had three layers was used for the first cut as it wasn't needed to perform the tests. The samples obtained were not satisfying because they weren't perfectly straight so that all of the samples didn't have the same width.

To prevent this problem, a guide has been added, the machine used is shown at figure 2.23. This guide also ensures that the cut is perfectly parallel to the fibers direction. The samples made are about 10 cm long in order to have a 2.5 cm margin at each roller support. When the test will be done, the roller will stay at the same place but the sample will move a little bit and this margin prevents the sample to fall out of the support.

Figure 2.23: Grinder machine used to cut the samples

2.8 Experimental tests

The three-point bending tests are performed on a MTS Criterion C43.504 machine. This machine allows to perform a lot of different tests such as tensile tests, compression tests or different kind of flexion tests. The configuration selected is shown at figure 2.24.
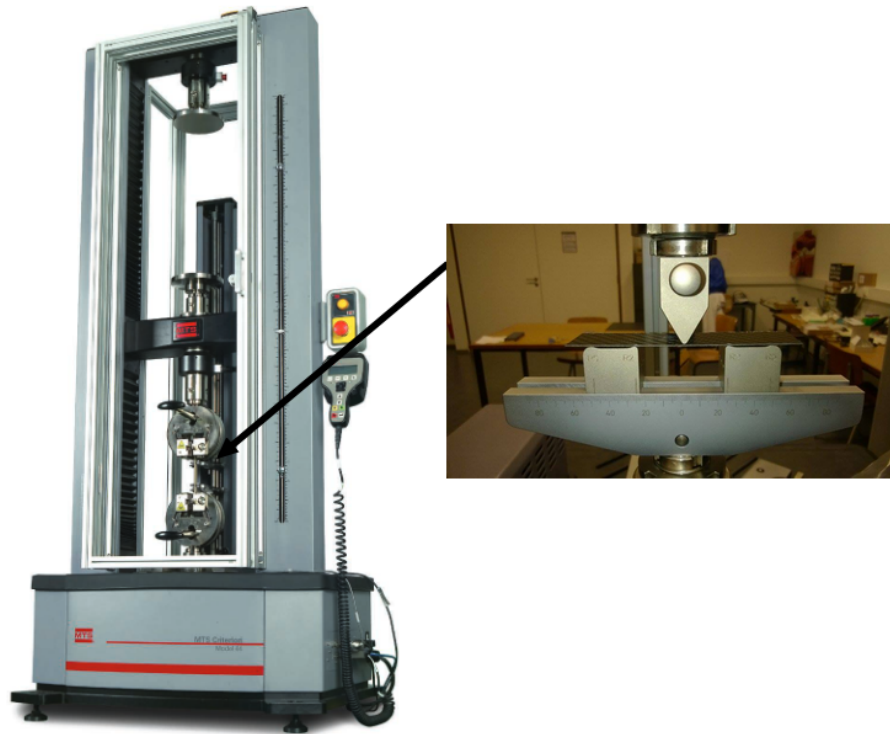
Figure 2.24: Machine used to perform the tests

The pin at the middle is going down, and the force detected by the machine is close to 0 until it touches the sample. The program detects that the pin touches the sample when the force applied is higher then a minimum value set by the user. In our case, the force to detect the sample is set to 0.15 N. At the moment the force reaches 0.15 N, the crosshead displacement is set to 0 mm and the force-deflection graph is plotted. The descending roller will descend at a speed of 0.05 mm/s. This speed is chosen low enough to simulate a static loading as our finite element model is static. A first test had been made with a descending speed of 0.2mm/s and the results were pretty bad as it was too fast. The samples tended to slip from the support leading to a non linear and chaotic graph.

The graph found for every sample is shown at figure 2.25.
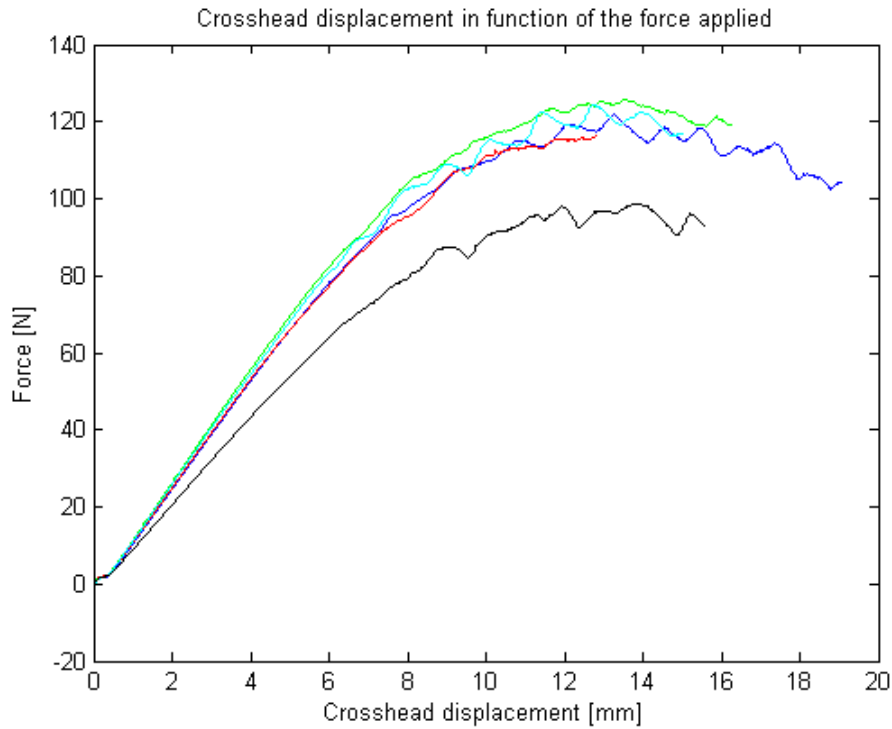
Figure 2.25: Curves representing the crosshead displacement in function of the applied force

The first thing to notice is that one of the sample gave some completely different results than the others. The real cause of this different result is hard to identify but a few reasons can lead to it. The sample might have been damaged during the manufacturing of the samples leading to a decrease of its mechanical proprieties. The cut might not be perfectly parallel to the fiber direction. Another possible reason can be that the resin of the matrix is not well distributed everywhere, it is shown at figure 2.26. During the forming process of the composite sheet, the resin might not have been applied everywhere in the same way, leading to an imperfect materials.
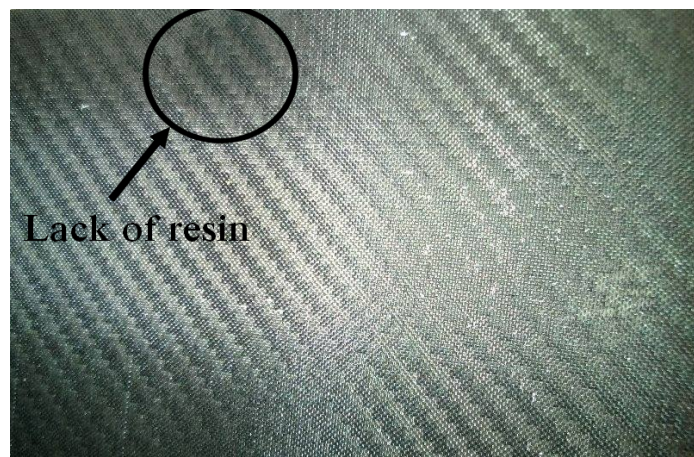
Figure 2.26: Example of a lack of resin on the composite sheet provided

We can see that the curves have a non-linear behavior at the beginning before becoming linear in the "elastic zone". This is underlined at the figure 2.27. As the samples are not perfectly flat, the contact zones between the samples and the supports are not perfect, then a tiny force has to be applied to push the sample on the supports and make a line contact between them. This non-linear zone at the very beginning of the graph can be ignored, this is made by removing the data under 0.29 N.
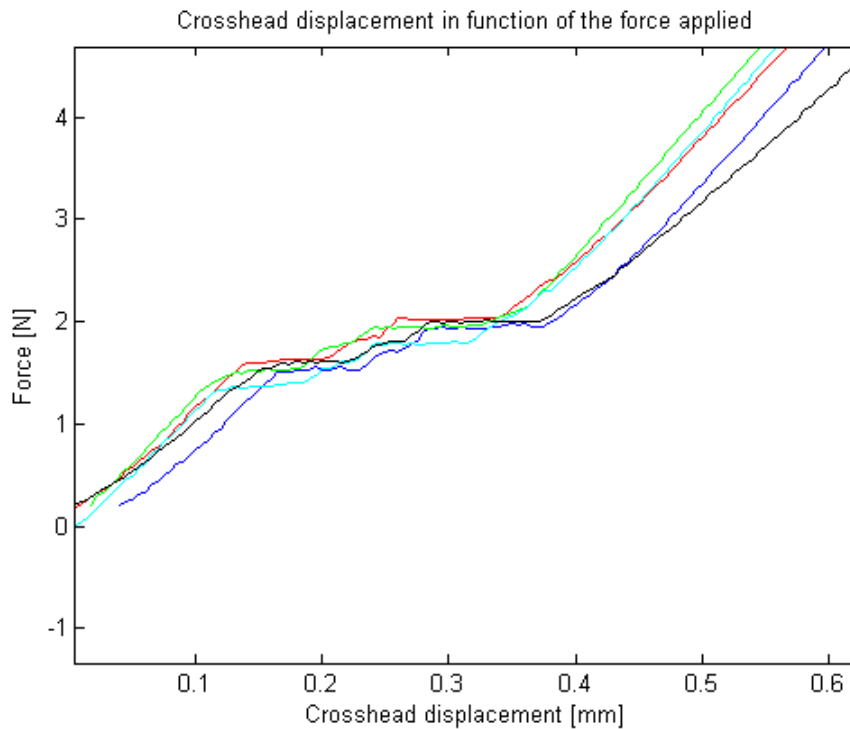
Figure 2.27: Non linear behavior for a force smaller then 0.27 N

Initially, the samples had to be broken during the test to validate the data used in the finite element model and validate the failure criteria. One sample have been broken and it exploded everywhere in the lab, then the next samples were not broken for a safety reason. As explained before, this is not a real problem as the limit of our model corresponds to the end of the linear behavior.

We can see that a non linear behavior occurs over 80 N. This value is slightly higher than the one that was found during the finite element simulations (70 N). Then our criteria used to detect the end of the linear behavior is assumed to be a bit more restrictive than the real behavior.

The shape of the curve in the non-linear zone has the typical shape of a material which is undergoing effects like plastic deformations or damages. Some bumps can be seen, the hypothesis to explain it is that the deformations were becoming too high and the samples tended to slip from their supports. The sudden slip explains those brutal changes of deflection followed by a "stiffening" of the material. The bumps are assumed to result from the imperfection of the support rather than a mechanical propriety of the material.

Manufacturer often gives the value of the flexural modulus to give an idea of the resistance to deflection of the material. From the force-deflection graph it is possible to plot a strain-stress graph. The formula from the simple beam theory are used but we must keep in mind that this theory is not adapted to composite and it is just used to have an idea of the material proprieties. The maximum stress and the maximum strain can be computed thanks to the following formula:

$$\sigma_{crosshead} = \frac{3FL}{2bh^2} \qquad (2.48)$$

$$\epsilon_{crosshead} = \frac{6Dh}{L^2} \qquad (2.49)$$

Where F is the force applied, L is the distance between the supports, d is the width of the samples, h is the thickness of the samples and D is the crosshead displacement.

From those equations, the stress-strain graph can be plotted for each samples and the slope of the linear part of the curve can be computed to find the flexural modulus.

Figure 2.28: Stress-strain graph of the samples
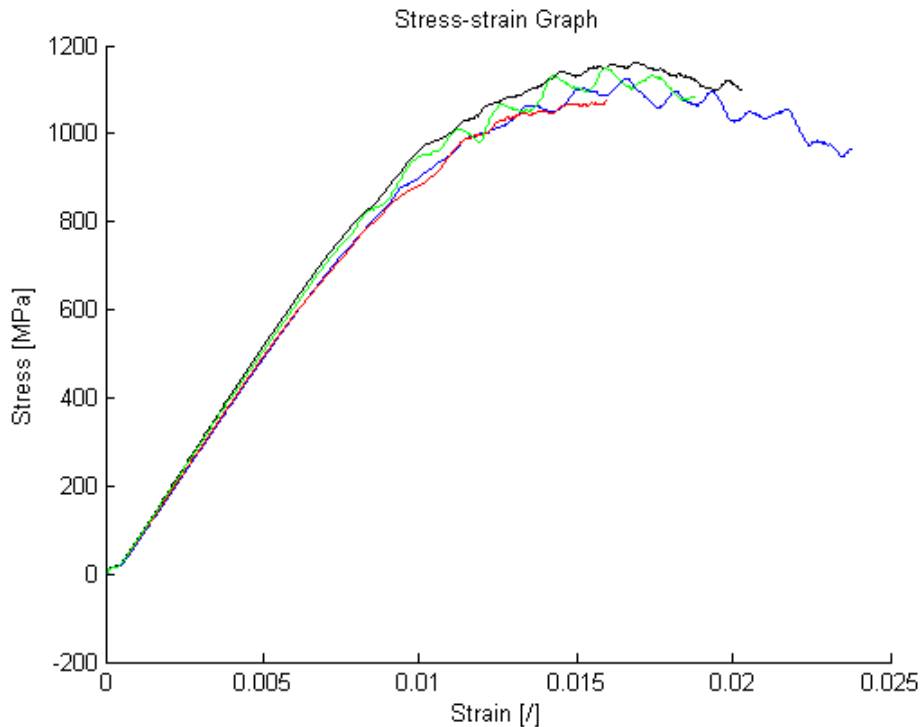
The flexural modulus found are about 105 MPa while the value of the provided by the manufacturer was 120MPa. Those values are satisfying, the samples responds as expected.

2.9 Comparison of the results

The force-deflection graph of the experimental tests and the finite element model can be superposed to see if they concur. The graphic found is shown at figure 2.29
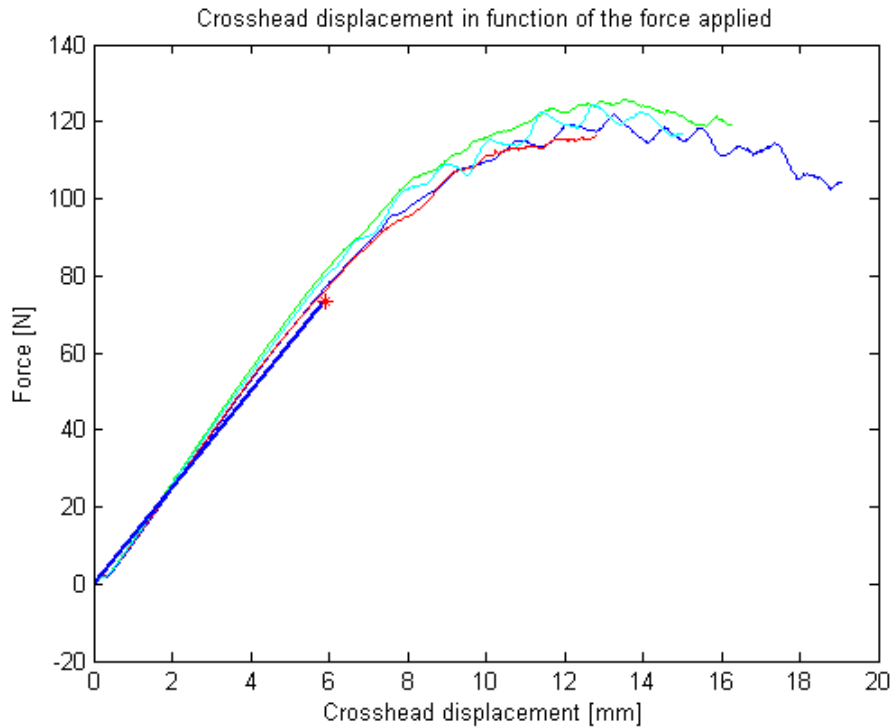
Figure 2.29: Comparison of the behavior of the experimental tests and the finite element model results

We can see that the slope of the linear part of the curves are almost the same, the real samples are just a little bit stiffer. The error of the finite element model concerning the displacements is about 2%. We can conclude that the Young's modulus used in the finite element model are correct.

We can also notice that there is a small offset between the experimental curves and the finite element model one because of the short non linear zone of the real samples.

A red cross is placed were the value of the Tsai-Hill criterion was equal to 1 in the finite element model. The Tsai-Hill equals 1 a bit before the end of the linear behavior of the real samples. This means that the yield strength values used mark the end of the linear elastic behavior of the material and not it's fracture. Then the values of the tensile and shear strength are validated. We can keep in mind that the non linear behavior of the real samples was reached a little bit later. It means that the strength values provided by the manufacturer were a bit pessimistic but it constitutes a great margin of security.

By those experimental tests, the mechanical proprieties of the T700S carbon fiber composite are validated.

Chapter 3

Finite Element Model of the UAV

Now that the proprieties of the composite material are known, the finite element model of the whole drone can be studied. A model of the drone is built on Catia which is a computer aided design software developed by Dassault. The model is then imported as a Brep file (model represented as surfaces stitched to each others) in Samcef. This is developed and a simple experimental test in flexion is performed to check its validity.

3.1 Geometry

The first step in the development of the finite element model is to have good geometries which leads to great meshes and which is representative of the reality.

Refiteh developed a 3D model to design the mold used to give the right shape to the composite sheets. This model is shown at figure 3.1. Initially this model should have been used in Samcef as it had a lot of advantages. Developing a new model would have take a lot of time and this one had exactly the same geometry than the real drone. However, for a few reasons it had to be changed.
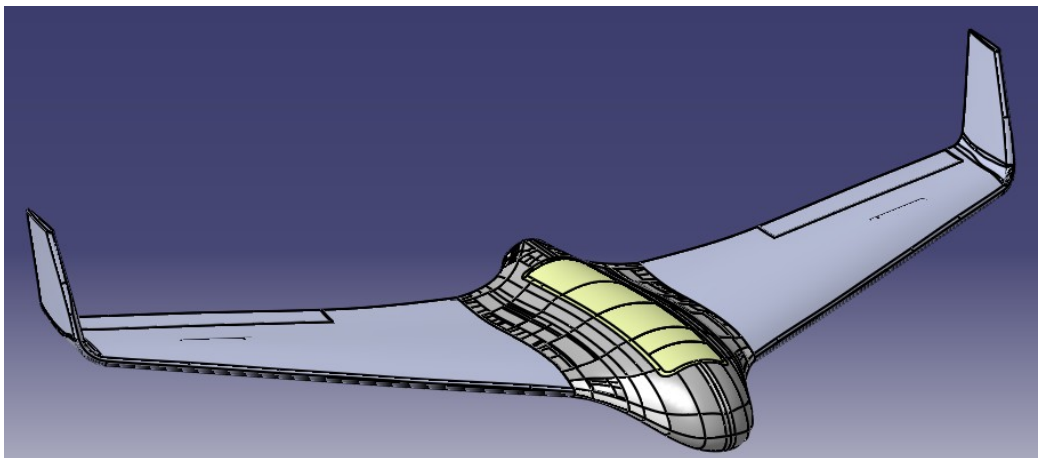

Figure 3.1: Modeling of the drone in Catia

The first problem was due to the way the model had been done. The society used a 3D scanner to build the model. This method is useful as it is fast and accurate but the resulting model is made of a lot of tiny faces and edges, especially at the leading edge of the wing and on the fuselage. This is shown at figure 3.2. It causes troubles in Samcef during the meshing of the structure. Samcef is forced to mesh every edges with at least 2 nodes, one at each end. This makes the mesh chaotic and irregular as some edges were way smaller then the averaged distance between the other nodes.
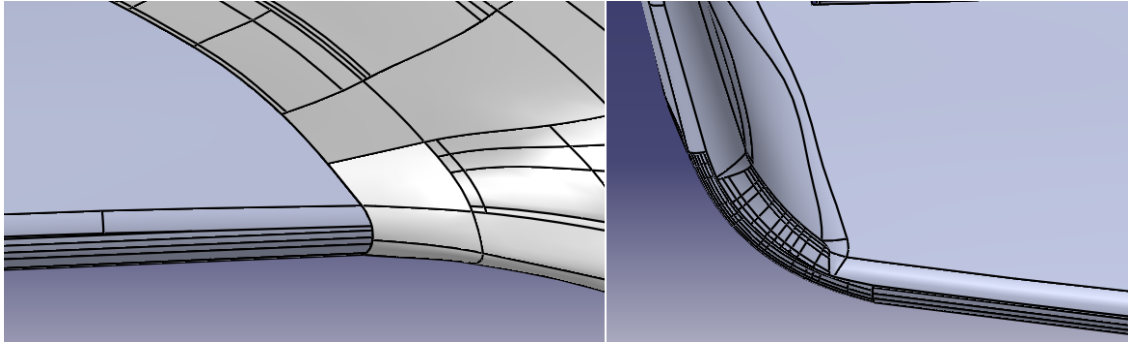
Figure 3.2: Complexity of the Catia model

The second problem was that the model was made of surfaces, during the importation in Samcef, the surfaces were not connected to each other. Connecting them in Samcef was possible by using boundary conditions but it would have been a long task as the number of faces is important. This problem is easily solved by importing a solid model from Catia and it prevents the possible errors that could have been done by setting the boundary conditions manually.

The geometry is changed in Catia in order to have less faces and a smoother mesh. The leading and trailing edges of the wings are replaced by simpler surfaces and the connection between the wing and the winglet is also simplified. Those changes don't change the geometry of the drone but it simplify the complexity of the model a lot. The new geometry can be seen at figure 3.3
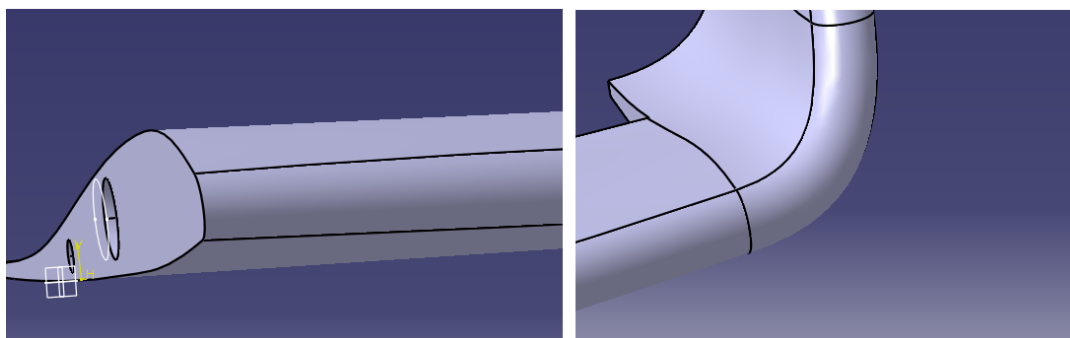
Figure 3.3: Simplified Catia model

The last thing to change is not a real problem but a smarter way to work. As the drone has a symmetry along the Y-Z-plane, it is possible to only work with a half drone and simulate the symmetry by using the right boundary conditions at the middle of the fuselage. It

makes the computation way faster as the mesh will contain two times fewer nodes. Locking the displacements along the Y-axis will simulate this symmetry. The hypothesis of a symmetrical configuration is not valid if the plane is flying with a sideslip angle for example. In such a case, the aerodynamic loads are not the same on the right and the left part of the drone. However, these flight configurations are not studied in this analysis and the hypothesis of a symmetrical air flow and a symmetrical distribution of the loads can be used.

Some simplifications can be added to the model to make the simulations easier. The first one concerns the ailerons. The ailerons are connected to the wing by a thin membrane. It can be considered that there is almost no interaction between the wing and the aileron so that the ailerons can be removed. The pockets on the wing which are containing the servos are covered by a thin plate of carbon fiber composite. With the hypothesis that it doesn't carry any efforts, they can be removed too. This hypothesis is also used to remove the hood of the fuselage.

The model cannot be built in one piece, a few pieces are built alone and they are assembled later in Samcef. The main parts to model are obvious, there must be the fuselage, the wing, the support inside the fuselage where the wing is attached and eventually, the bar which connects the wing's part to the fuselage.

The support is not built by Refitech so no 3D model of it was available. It has been modeled manually in Samcef. The support is made of a L-shape shell made of carbon fiber composite and a cylinder made of aluminum alloy and is inserted in the fuselage as it is shown at figure 3.4. The model used to represent it is shown at figure 3.5.

Figure 3.4: Presentation of the support in the UAV

As it can be seen on the picture, the cylinder is actually attached to the composite shell thanks to two rivets. However, in the finite element model, rivets are hard to model, then the contact between them is made linear but we must keep in mind that the real stress will be higher at this place as the rivets produce a concentration of stresses.

Another part needs to be built, indeed, the wing are filled with polyurethane foam and it is not possible to represent the skin and the foam inside it with a single object. Then the model

used for the skin is duplicated and converted to a solid element which has the properties of the foam, the interactions between the foam and the skin are simulated later.

The final geometry of each elements is shown from figure 3.5 to figure 3.8.
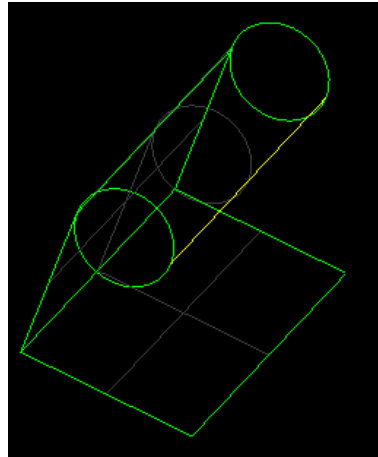
Figure 3.5: Model of the support used in Samcef
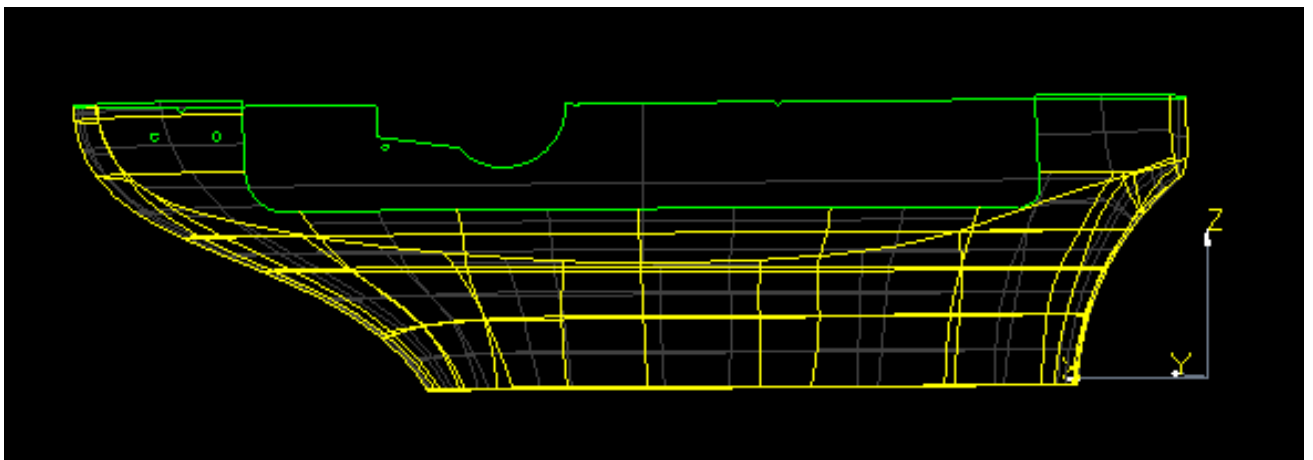
Figure 3.6: Model of the fuselage used in Samcef
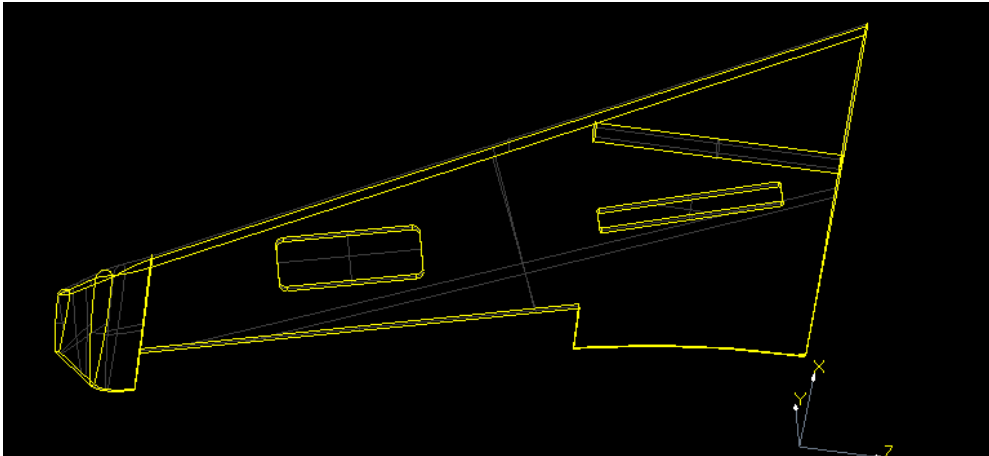
Figure 3.7: Model of the wing used in Samcef
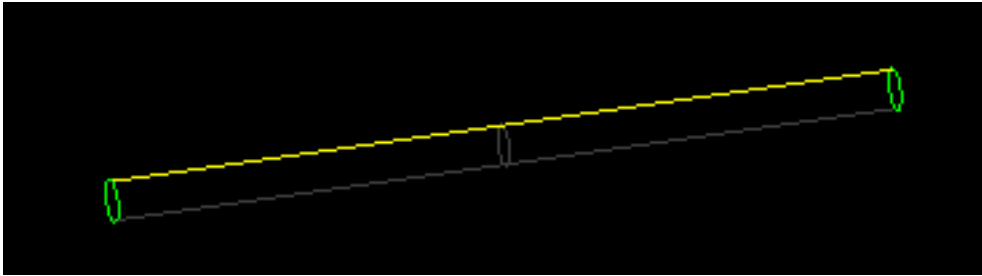
Figure 3.8: Model of the composite bar used in Samcef

To sum up, the different bodies are the following and they are connected together thanks to the boundary conditions expressed below:

-The composite shell of the wing: This is a shell element which models the carbon fiber composite skin.

-The solid model of the wing: This is used to model the foam inside the wing. It is connected to the skin by gluing the elements of the skin to it.

-The fuselage: Shell elements are used to represent the composite skin.

-The support : The support is fixed to the fuselage by using the "gluing" option.

-The carbon fiber composite bar: It is modeled by a shell element. The bar is fixed to the wing thanks to the foam, gluing it inside the solid model of the wing simulate it. It is connected to the support by adding a "contact" constrain between them.

It is important to notice that there is a fundamental difference between gluing elements together and simulating a contact between them. Gluing means that the elements are attached together, then the nodes at the interface of the two objects will follow the same displacements. The contact only means that they are touching each other, there is an interaction between them only if the first element applies a pressure on the second one, if a tension is applied between two element which are in contact, there will be no interaction between them. The contact constrain is perfect to simulate the contact between the support and the bar while the glue option would have lead to the wrong constrains and displacements.

A few more boundary conditions are added to make the model more realistic. A contact constrain is added between the side of the fuselage and the extremity of the wing (see figure 3.9). Indeed, in reality the wing and the fuselage are not only connected together by the bar, they are touching each other and this zone is susceptible to generate high constrains. As the drone is still in development and was still at the prototype stage when the analysis was performed, the wing and the fuselage were touching each other directly as it is shown at figure 3.9. A joint will be used in the commercialized model to avoid a direct contact between the composite parts. Rivets were not considered in the model, however, it is needed to model the rivet which is at the front of the wing. It connects the wing to the fuselage and unable the rotation of the wing during the flight. It is modeled by gluing a few nodes of the wing to the fuselage.

Figure 3.9: Direct contact between the wing and the fuselage on the prototype UAV

The final model used is shown at figure 3.10
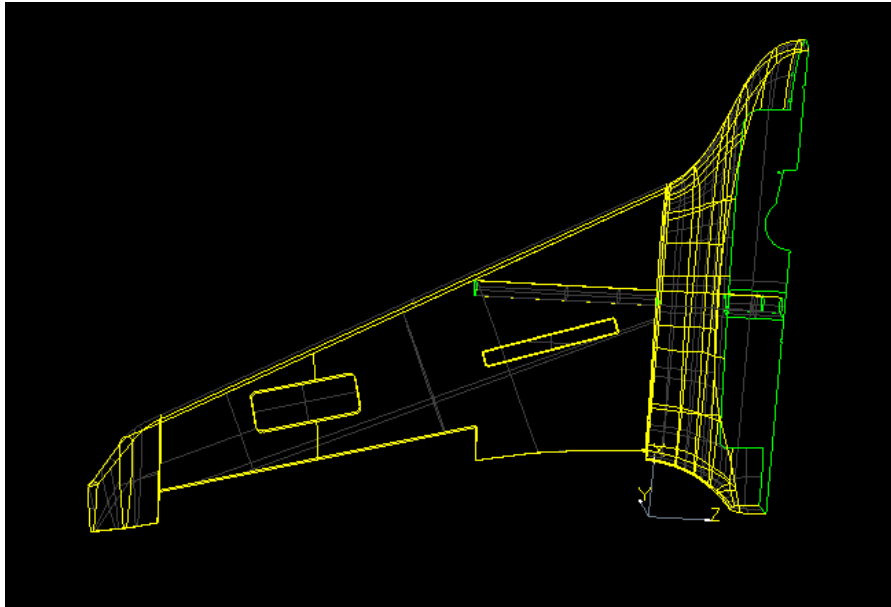
Figure 3.10: Complete model of the UAV in Samcef

3.2   Materials

To finish the model, the proprieties of all the materials needs to be set.

The skin of the wing and the fuselage are made of T700S carbon fiber composite. It has been studied in the previous chapter the proprieties have been verified by an experimental test. Those proprieties are available in the figure 2.12.

The composite bar is made of the same material except that the sheets are thicker (0.33mm per sheet), the total thickness is 2 mm while the outer diameter is 25 mm. Then, the proprieties of the material of the bar are the same as the skin, only the thickness of the layers changes.

The support which connects the wing the the fuselage is made of a L-shape piece attached to a cylinder made of aluminum alloy. The thickness of the composite piece is 2.5 mm and it has the same proprieties then the composite used before. The cylinder has an inner diameter of 25 mm and a thickness of 2.5 mm. However, its inner diameter is changed by 1 mm for practical reason. If it was set to 25 mm, it would have correspond exactly to the diameter of the composite bar, there would not have been any space to fit them together in the model. Adding a 1 mm margin allows us to suit the composite bar into the support. The documentation about the aluminum alloy is easy to find and the data used are:

Thickness of the shell	2 mm
Mass Density	2700 kg/m^3
Young's Modulus	70e3 MPa
Yield Strength	241 MPa
Poisson ratio	0.32

Figure 3.11: Proprieties of the aluminum alloy

Eventually, the polyurethane foam has to be studied. Working with foam is pretty annoying as its proprieties depend of a lot of factors. First of all, its proprieties depends on the expansion direction of the foam. Indeed, two substances are injected inside the wing which is still in the mold and a chemical reaction occurs which expends the foam. The process to inject the foam in the wing is delicate. At first, the foam was injected directly in the wing without any precautions but the pressure it applied on the skin deformed the wing a lot. In order to prevent the deformations, the wing is placed in a mold which prevents the deformations and the foam is injected. The way the foam is injected in the wing can change its proprieties, some spot in the wing might even have no foam.

It is also not rare to find a negative value for the Poisson ratio. This is due to the fact that the foam is a very porous material.

The anisotropic behavior of the foam is shown at table 3.12. This table contains the detailed data collect by Dr Wit Witkiewicz and Dr Andrzej Zielisky [12] for a $62kg/m^3$ polyurethane foam. We can clearly see that the proprieties of the foam depend on the direction of the foam rise.

Density	62 kg/m^3
Compressive strength parallel to foam rise	0.64 MPa
Compressive strength perpendicular to foam rise	0.41 MPa
Compressive modulus parallel to foam rise	19.5 MPa
Compressive modulus perpendicular to foam rise	10 MPa
Tensile strength parallel to foam rise	26.7 MPa
Tensile modulus parallel to foam rise	12.3 MPa
Tensile modulus perpendicular to foam rise	0.34 MPa
Tensile modulus perpendicular to foam rise	0.36 MPa
Shear strength in plane parallel to foam rise	6.4 MPa
Shear strength in plane perpendicular to foam rise	6.2 MPa

Figure 3.12: Proprieties of a polyurethane foam

The Poisson ratio of such kind of foam are usually considered as very small. As we can see in the previous table, the Young's modulus of the foam is very small and it's role is actually to prevent the deformation of the airfoil of the wing. Almost all the stresses are carried by the composite skin and the bar. It will be shown in the finite element model that the foam is not

carrying a lot of stresses. We can see our wing as a double T beam were the parallel flanges are carrying the stresses while the web is simply keeping the flange away from each other.

The last problem is that the behavior of the foam changes if it is working under compression or in traction. The behavior in traction is almost linear. However, in compression, it can be different. A typical stress-strain graph in compression for a foam is shown at figure 3.13.
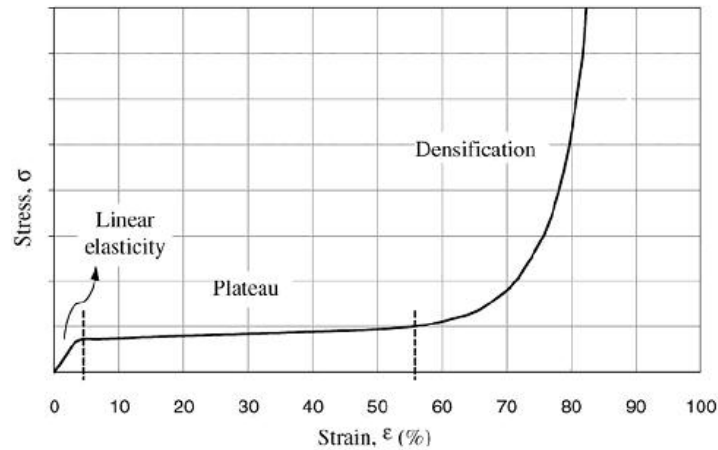

Figure 3.13: Example of a stress-strain graph of a foam

The first part is linear, until it reaches a plate. After a maximum stress, the material is stiffening suddenly. This is because the foam is full of air. During the beginning of the compression, the material is very porous. Deformations undergo until all the tiny holes inside the foam are compressed, from this moment, the material is not porous anymore and the material is stiffening. This behavior is called the densification as the density of the material changes during the loading. In our case, as the deformations remains small, the behavior is assumed to be linear and to be the same in compression and traction.

To sum up, the foam can be considered as an isotropic material with a small Poisson ratio. The Young's modulus can be extracted from the figure 3.14[6]. This figure presents the Young's Modulus of the foam in function of its density. In our case, the density is $42 kg/m^3$ and the corresponding Young's modulus is 26 MPa. In comparison, the Young's modulus of the carbon fiber composite was 125 GPa in one direction and 13.3 GPa in the others, there is a factor 1000 between them. We can understand from this difference that the role of the foam is not the carry the effort but simply to avoid the deformation of the skin.
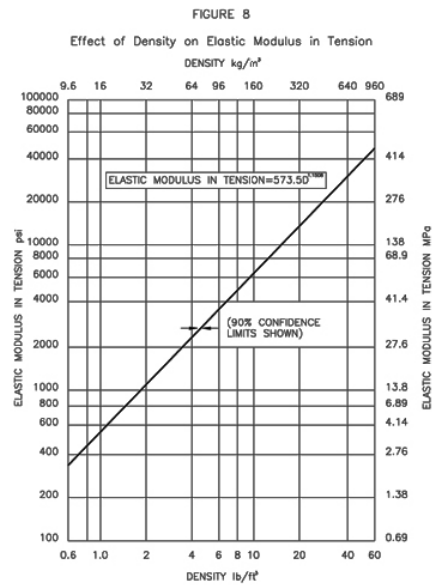
Figure 3.14: Tensile Young's modulus in function of the density of the foam [6]

3.3 Experimental test

A simple experimental test is performed to check the validity of the model. At first, the test should have consist in clamping the fuselage and applying a vertical force at the end of the wing. However, clamping the fuselage is a hard task and a simpler test has been chosen.

The drone is supported at each end by roller supports. Some weights are placed in the fuselage near the center of gravity and the deflection is measured. A photo of the test is shown at figure 3.15.
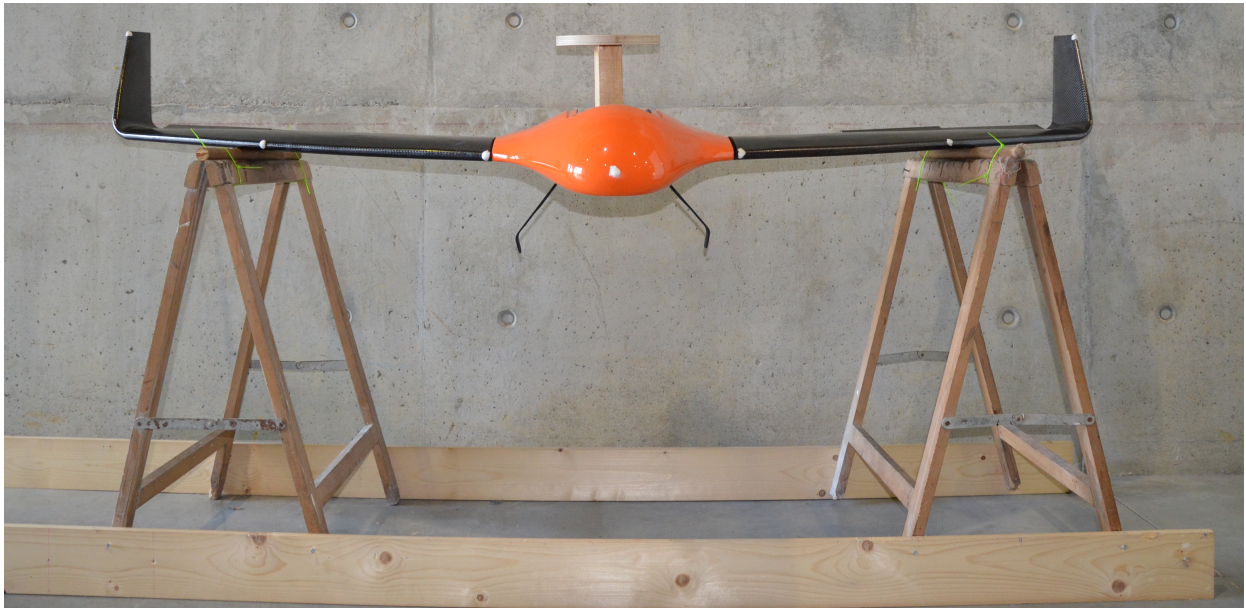
Figure 3.15: Configuration of the experimental test

At first, the supports were supposed to be placed at the tip of the wing in order to measure the highest deflection possible. However, in practice, when the plane is placed on the support, it cannot stay in a stable position and it tends to fall on its nose. It is due to the position of the center of gravity. As the wing are swept backward, the plane was supported by two points located behind the center of gravity. The configuration is shown at figure 3.16.
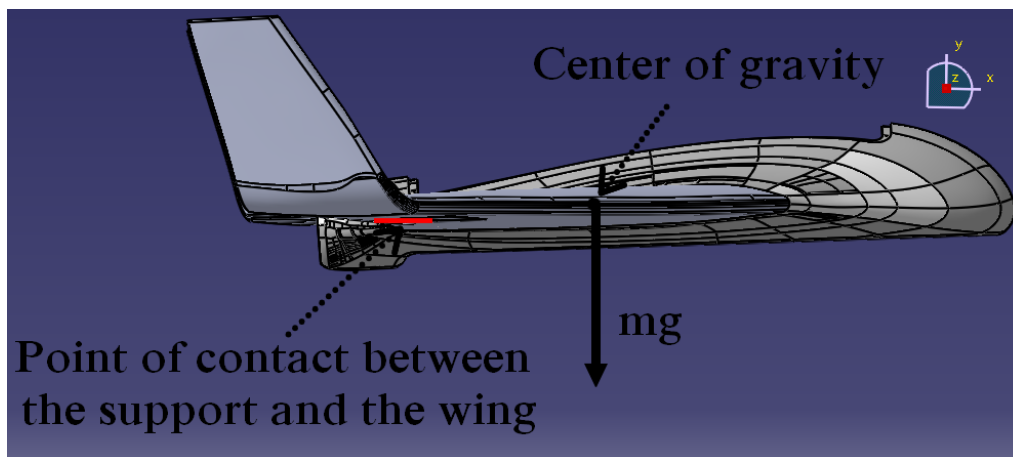
Figure 3.16: Side view of the configuration leading to a rotation of the drone

Diminishing the distance between the supports allows to align the center of gravity and the position of the support along the X-axis (see figure 3.17). Aligning them also ensure that almost no torsion will occur during the tests and allows us to work in the Y-Z plane.
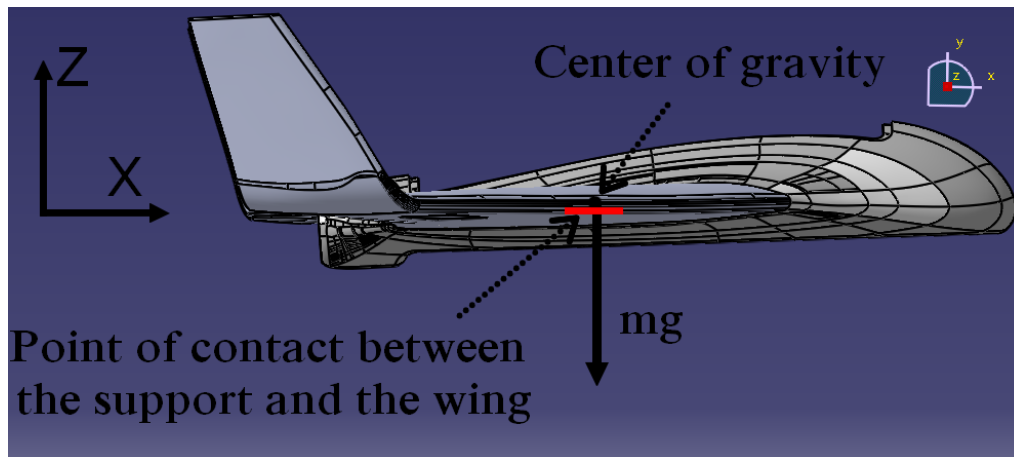
Figure 3.17: Side view of the final configuration

The final configuration in the Z-Y plane is the following:
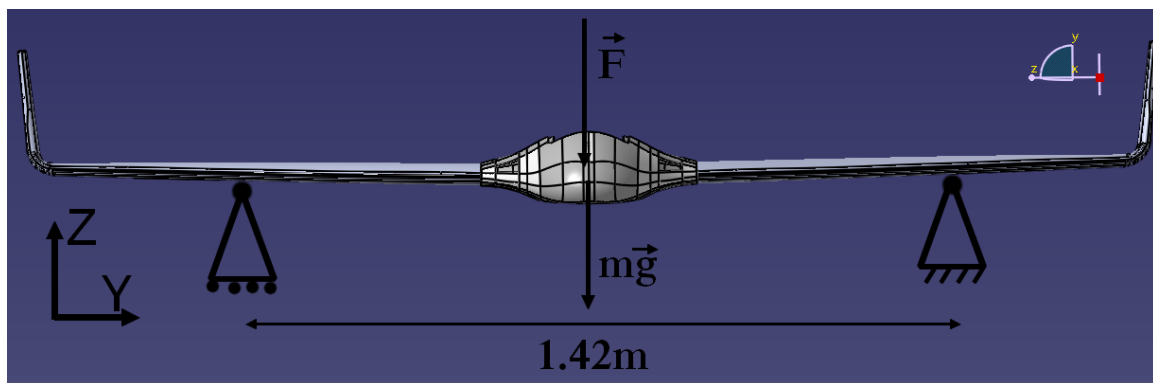
Figure 3.18: Front view of the final configuration selected

The force is applied on the fuselage by adding some masses around the center of gravity. This force needs to be applied at the same spot all the time. To do it a wooden support is designed and is shown a figure 3.19. Its shape allows it to be fixed inside the fuselage, the plate at the top supports the weights which wouldn't have filled in the fuselage. With this configuration, the different weights are added and always apply a pressure on the same surface at the bottom of the fuselage.
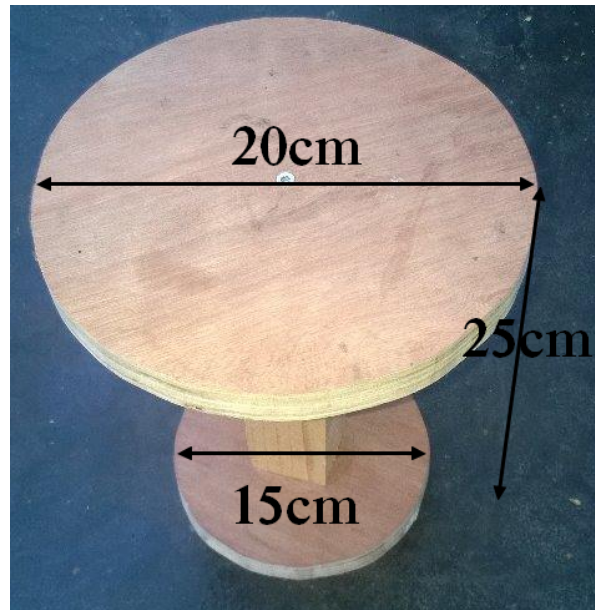
Figure 3.19: Design of the wooden support

The roller supports were build with trestles, round pieces of wood are added at the top to simulate the boundary conditions of the finite element model as well as possible. The trestles are attached to each others in order to prevent their displacement. Indeed, applying a force on the aircraft will deform it and it will tend to push the supports away from each other. The whole configuration was shown at figure 3.15.

The best way to measure the displacement would have been to use a laser as it would have been very accurate. In our case, a high resolution camera was placed in front of the plane. A picture is taken for every different forces applied and the pictures are post processed to compute the displacement. The main problem of this method is that it induces some errors due to the parallax. To minimize it, the camera is placed at the same height then the plane. The test is performed twice by resetting the position of the camera to minimize the error. White dots are marked on the drone to follow the displacement of the same point in each configuration. The wooden support is also used as a reference to compute the displacements. The force applied is increased by adding masses on the wooden support. The pictures are analyzed afterward with a software such as *Photoshop*. It allows to find the coordinate of a pixel, in our case, the three points followed are shown at figure 3.20.

As the force is aligned with the center of gravity along the X-axis, the drone should not rotate and the displacement of the point 2 and 3 should be the same then the displacement of the bottom of the fuselage. As all the dimensions of the drone are known it is possible to find the ratio to convert a displacement in pixels into a displacement in mm. Two known lengths are used and the ratio used is the mean of the two ratios found. The reference lengths are the span of the drone and the thickness of the fuselage. The final ratio found is :

$$1 pixel \Rightarrow 0.48 mm \tag{3.1}$$
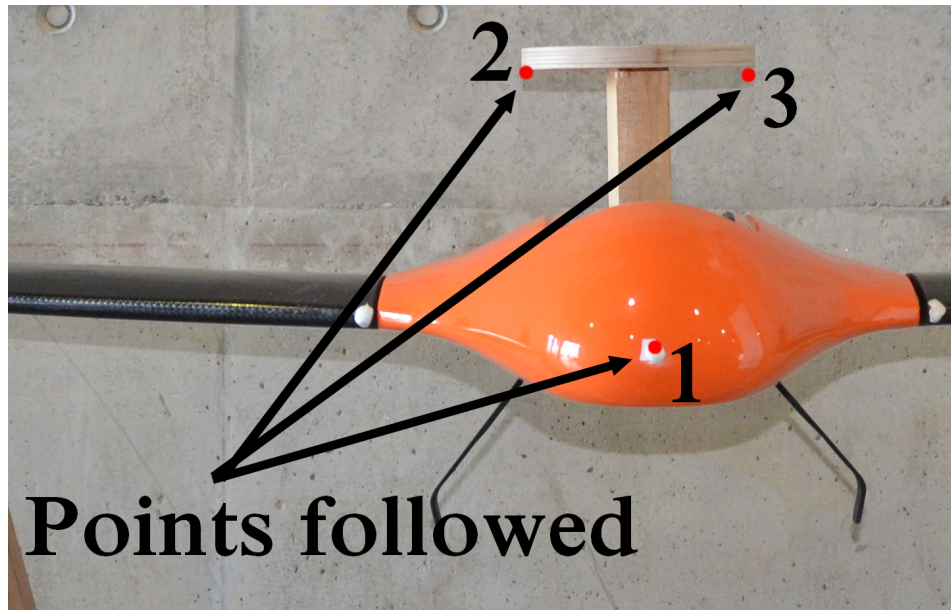
Figure 3.20: Points followed during the test

The pictures can be analyzed and the displacements found for the first test are shown in the table below. At first, all of the displacements are computed from the configuration when there is no applied force. The results are shown at figure 3.21.

Mass added[kg]	Resultant force[N]	Disp. pt1 [mm]	Disp. pt2 [mm]	Disp. pt3 [mm]
0	0	0	0	0
3	29.4	17	-2	-4
6	58.9	13	-12	-13
8.5	83.4	7	-21	-22
11	107.9	-7	-35	-34
13	127.5	-15	-40	-41

Figure 3.21: Table of the displacement of the first test computed from the 0 kg configuration

The first thing to notice is that the displacement of the nose seems to be not coherent. When a bit of weight is added, the nose goes up which is not an expected result. Actually, when the drone laying on the supports, it not in a stable position. A small force has to be applied which makes to drone rotate a little bit and eventually reaches a stable position. This small rotation makes the nose go up and explains the positive displacement of the point 1. For this reason, it is more interesting to look at the slope of the curves found or compute the displacement from the 3 kg configuration. The new results of the two tests are shown at figure 3.22 and 3.23.

This time, the displacements are indeed increasing when weight is added as expected. The force-displacement graph can be plot as the most interesting thing to compute are the slope of the force-displacement curves. This graph is shown below at figure 3.24. On this graph, the

Mass added[kg]	Resultant force[N]	Disp. pt1 [mm]	Disp. pt2 [mm]	Disp. pt3 [mm]
3	29.4	0	0	0
6	58.9	-4	-10	-9
8.5	83.4	-10	-19	-18
11	107.9	-24	-33	-30
13	127.5	-32	-38	-47

Figure 3.22: Table of the displacement of the first test computed from the 3 kg configuration

Mass added[kg]	Resultant force[N]	Disp. pt1 [mm]	Disp. pt2 [mm]	Disp. pt3 [mm]
3	29.4	0	0	0
6	58.9	1.46	-4.4	-4.8
11	107.9	7.8	-13.2	-13.2
13	127.5	11.7	-17.1	-17.1
16	156.9	17.5	-24.4	-24.9

Figure 3.23: Table of the displacement of the second test computed from the 3 kg configuration

displacements of the point of the nose are represented in red while the displacements of the points of the support are plotted in blue.
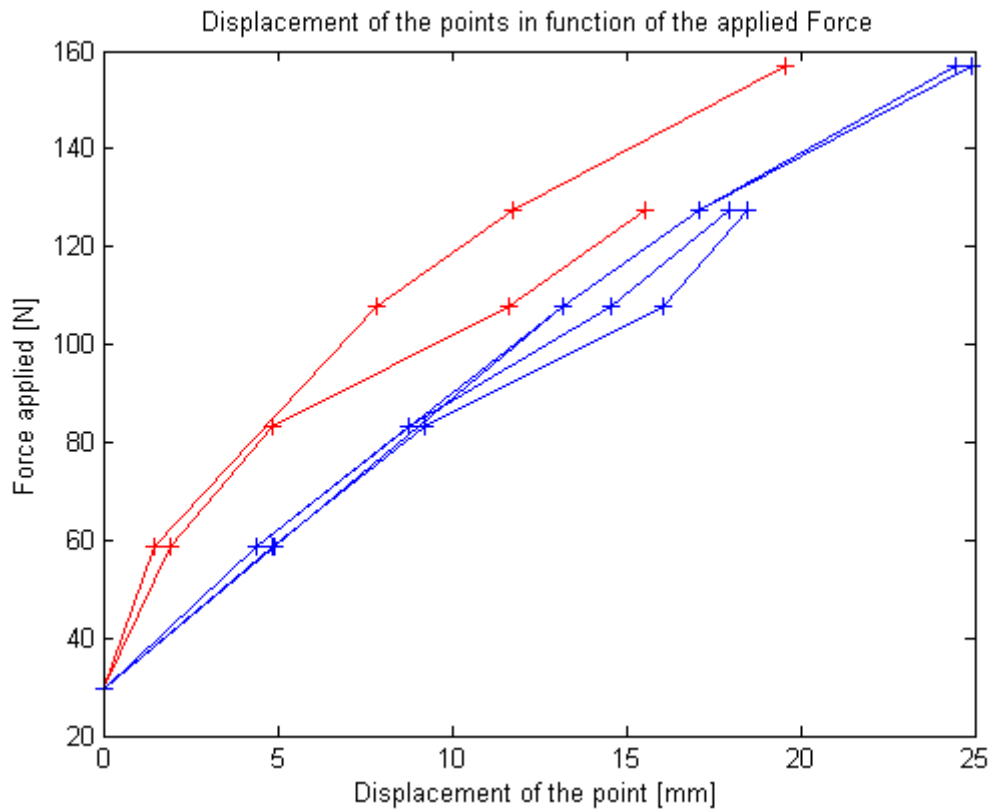

Figure 3.24: Force-displacement graph of both tests

We can notice that the displacements of the points of the support are almost the same and their curves are almost linear. The displacements of the nose are a bit different. The hypothesis to explain it is that the plane is doing a small rotation for every added force.

The displacement of the nodes of the support are almost linear which was the expected behavior. From now, the displacement of the points of the support will be used to calculate the displacement of the drone as the results were better and more coherent.

3.4   Finite element model results

As the geometry of the drone is already modeled, the right boundary conditions has to be added to simulate the configuration of the experimental test. The supports are considered as perfect roller supports, this is done by locking the displacement along the Z-axis at the location of the supports on the model. The force is applied by using a vertical surface force on a half disk attached to the fuselage (see figure 3.25). The surface force to apply can be simply computed as : $P = \frac{m*g}{\pi*r_{supp}^2}$ where m is the mass applied on the support, g is the gravity acceleration and r_{supp} is the radius of the wooden disk which applies the pressure on the fuselage. At the center of the drone, the displacement along the Y-axis is prescribed to simulate the symmetry. Eventually, the displacement along the X-axis is prescribed at one point of the roller support to remove the rigid body modes. Those boundary conditions are shown at figure 3.26 and 3.27.
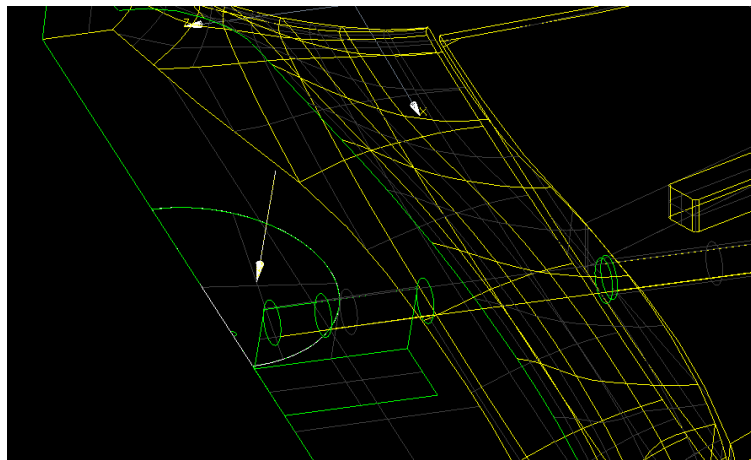

Figure 3.25: Simulation of the force applied on the fuselage

Figure 3.26: Boundary conditions used to simulate the symmetry of the drone
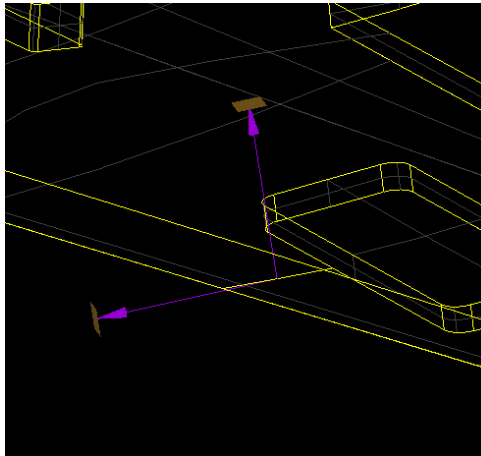
Figure 3.27: Boundary conditions used to simulate the roller support

As we are working with a simplified finite element model, only the general behavior of the drone is required, then the behavior is almost perfectly linear and three configurations are use to plot the force-displacement graph. The real behavior is actually non linear as there is a lot of interactions between the elements, the joints and the rivets. It wouldn't make sense to compute the deformations for a lot of different weights in the finite element method as it wouldn't give a great picture a the reality.

The force-displacement graph is plotted for a force equal to 0 N, 78 N and 157 N. The results are shown at table 3.28.

A graphic can also be plotted to compare the difference of slope between the experimental and the simulated curves. As it has been explained before, the slope of the curve is more important then the deflection itself. The curves found with the finite element model has been translated to be able to compare the slopes easily. The results can be seen at figure 3.29. The results of the finite element model are plotted in red while the real values are shown is blue.

Resultant force [N]	Disp. at the bottom of the fuselage [mm]
0	0
78	11.8
157	23.3

Figure 3.28: Displacements on the finite element model
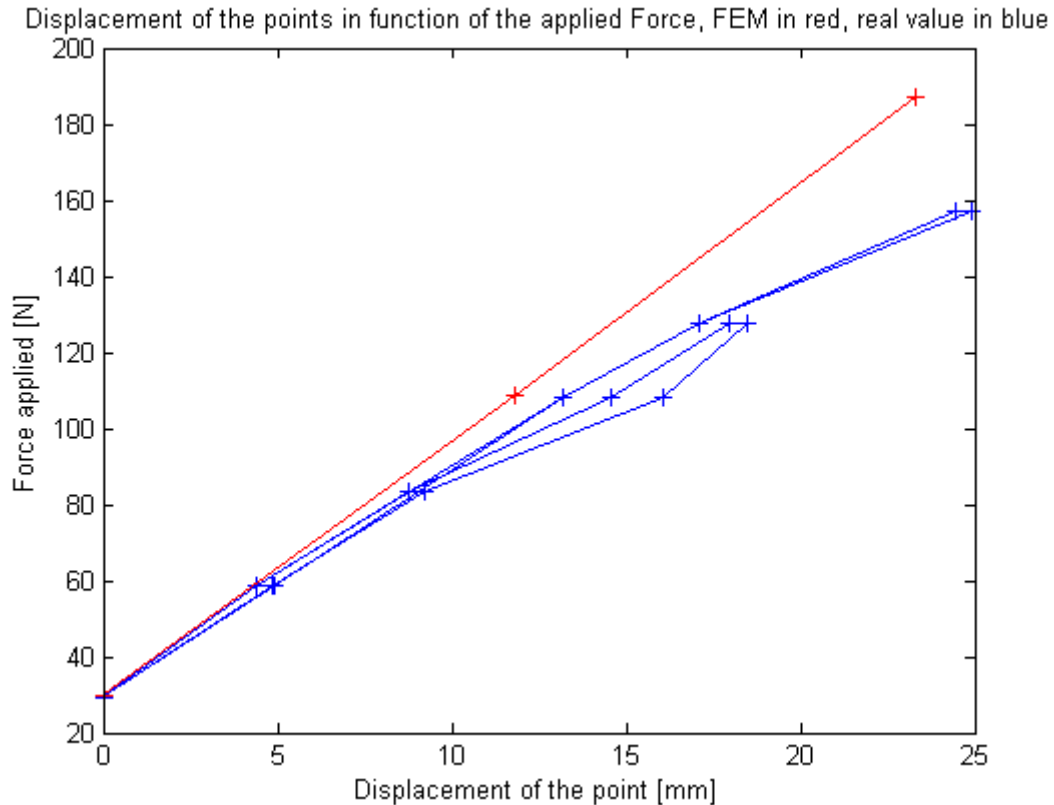
Figure 3.29: Comparison of the slope of the force-displacement curves

From this figure, it can be seen that the real drone is a bit more flexible as the deformations found are a bit more important. This is explained by the fact that the finite element model doesn't take the rivets or joint into account. Moreover as it was shown in the previous chapter, the proprieties of the finite element model lead to a composite material a bit more stiff than the real one.

If we take a look at the displacements on Samcef (See figure 3.30) we can notice that a small rotation of the fuselage is occurring as the nose of the fuselage undergoes less displacements than the bottom of the fuselage near the gravity center. This results seems to confirm the hypothesis made before concerning the displacement of the nose of the fuselage.

Figure 3.30: Displacement found on Samcef for an applied force of 78 N

Figure 3.31: Displacement found on Samcef for an applied force of 157 N

It is also interesting to look at the constrains of the finite element model. The constrains are studied in the case of an applied force of 157 N as this is the configuration which solicits the drone the most. The figure 3.32 presents the value of the Tsai-Hill.
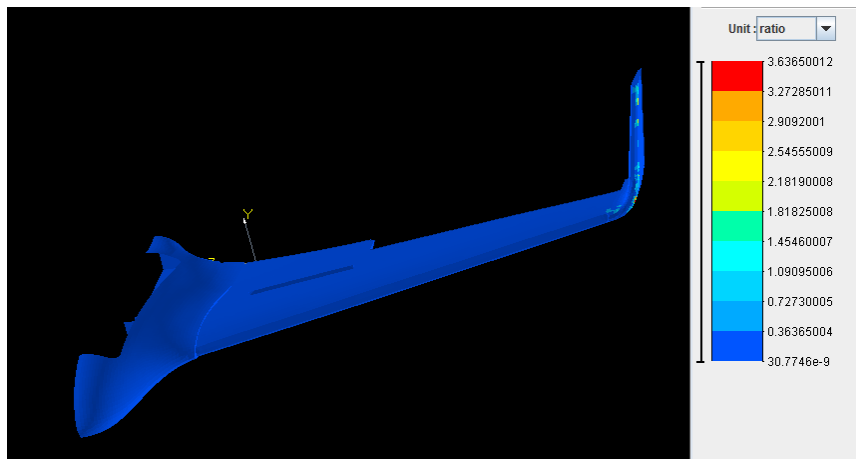
Figure 3.32: Tsai-Hill value for an applied force of 157 N
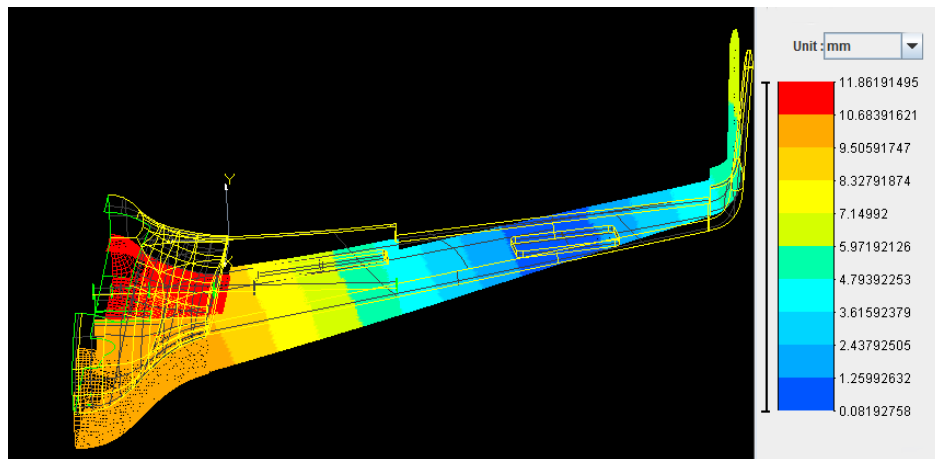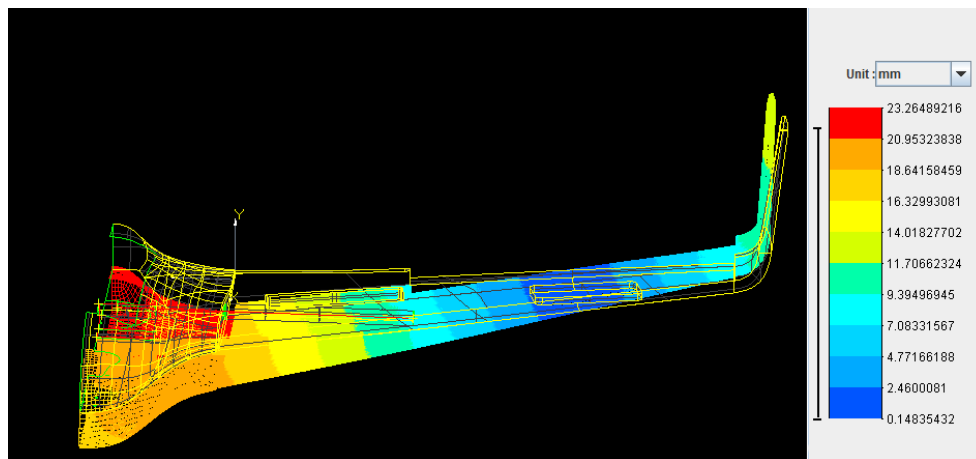
Something might look strange, indeed, if we take a look at the wing tip (figure 3.33), it can be seen that there are really high constrains in the skin while it should be close to 0 as no stress is expected there.
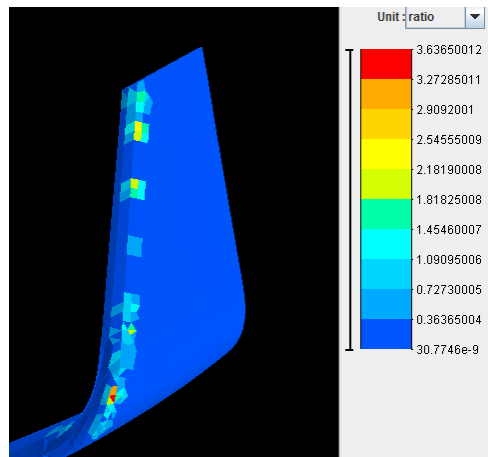
Figure 3.33: Tsai-Hill value end the wing tip for an applied force of 157 N

It's actually some errors due to the finite element method. At the interface between the foam and the skin, the software tries to ensure the continuity of the stress and the kinematic constrains. This problem is actually impossible to solve and a concentration of stresses is created by the software to solve it. The high stresses at the end of the wing are actually artificial and this problem is solved by removing the gluing constrains of this surface on the wing and changing it to a simple contact between the skin and the foam. The same thing is done at the leading edge by simulating a contact between the foam and the leading edge skin. Those changes do not change anything on the results except that it removes the artificial constrains. The constrains are now easier to see as they are scaled compared to the highest real stress.

The Tsai-Hill values of the new model are shown below:
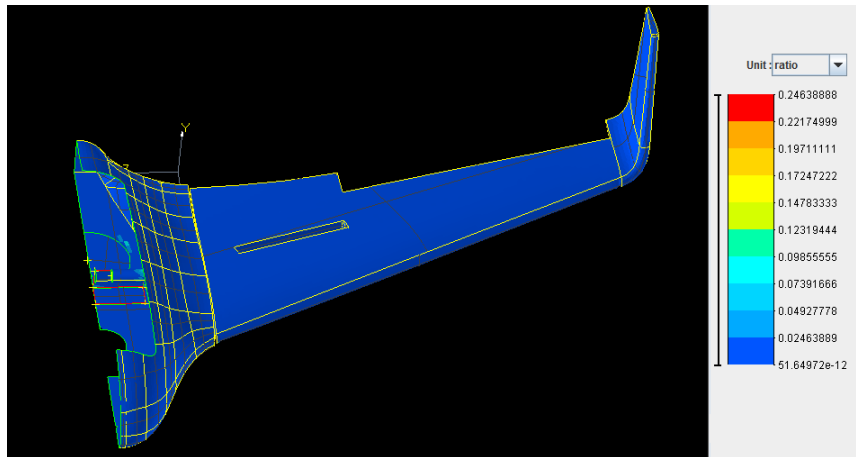
Figure 3.34: Tsai-Hill value for an applied force of 157 N

Now that the model is corrected, it is easier to analyze the stresses. The first thing noticeable is that the constrains on the skin of wing are tiny, this is due to the thickness used for the skin, even if it's 0.52 mm thick, this is still a very high value for a drone which is supposed to undergo small forces during the flight. This thickness is usually used for microlight aviation, the thickness for big planes is usually between 1 and 2 mm. Some spot are more interesting to study.

The first one is the interaction between the composite bar and the support. The mesh is very detailed at this spot in order to have a great idea of what is happening. The value of the Tsai-Hill is shown at figure 3.35 and 3.36. The Thai-Hill value is still small, it is because the thickness of the bar is enormous (2.5mm) for the size of the drone.
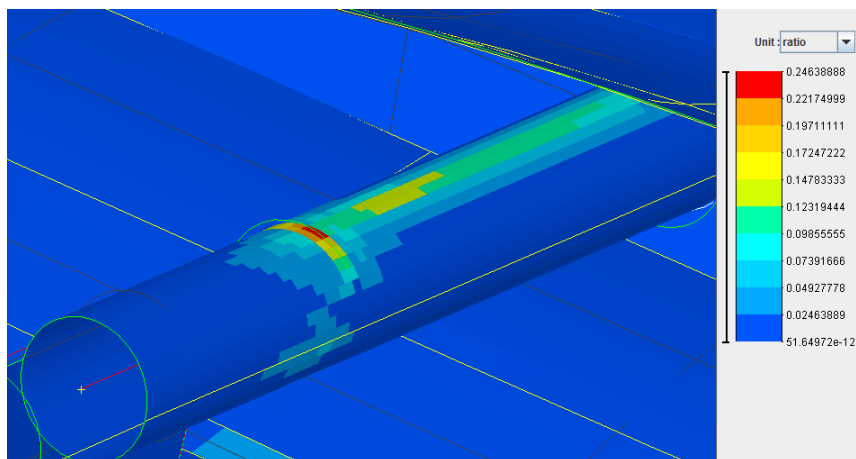
Figure 3.35: Tsai-Hill value in the composite bar
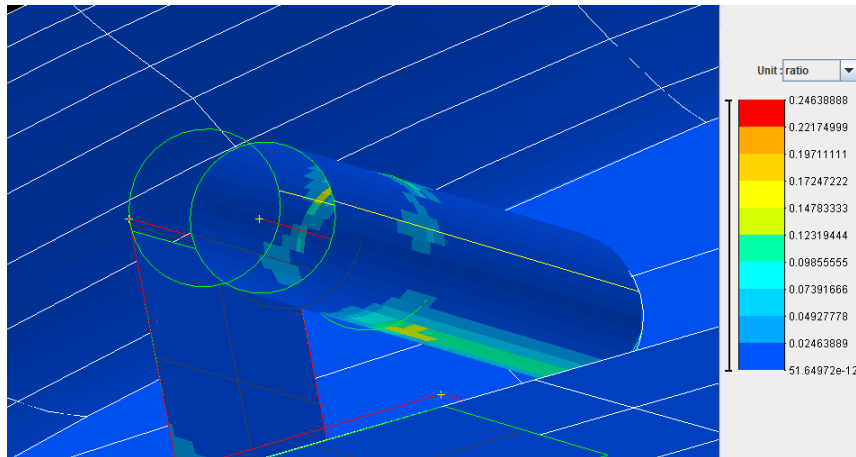
Figure 3.36: Tsai-Hill value in the composite bar

The bar is locking the displacement and is pushing on the support as expected. The spot where the constrains are the highest is at the end of the support.

The second interesting spot to watch is the zone where the support is attached to the fuselage (See figure 3.37). There is a little concentration of stresses. As the composite bar is pushing the support upward, the support also tends to pull the fuselage upward, those constrains result from this mechanism. However, the stresses on the support should be higher in reality. The support is not really glued to the fuselage and to the aluminum bar. Rivets are used which lead to a high concentration of stresses. As we are working with composite, a small imperfection while drilling the holes of the rivets can cause a significant increase of the stresses at those points when a high load is applied. For that reason, the experimental test is not going over a maximum force of 157 N, it allows to see deformations while staying far from the limit of the material.
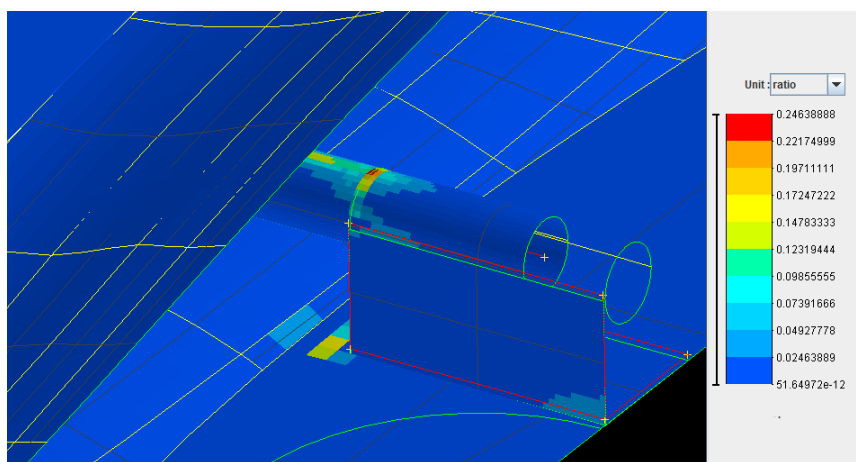
Figure 3.37: Tsai-Hill value at the bottom of the fuselage

The aluminum cylinder can also be studied, as this is an isotropic material, the von Mises equivalent stress is used and it reaches a maximum value of 54 MPa while the yield strength is

about 241MPa. The material keeps an elastic behavior as expected.
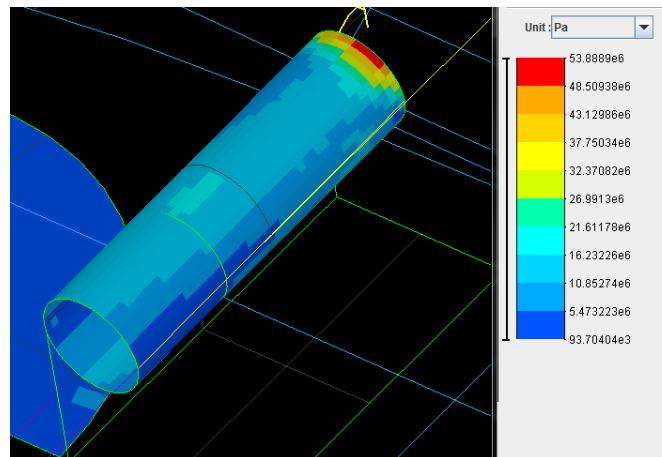
Figure 3.38: von Mises equivalent stress at the top of the aluminum cylinder
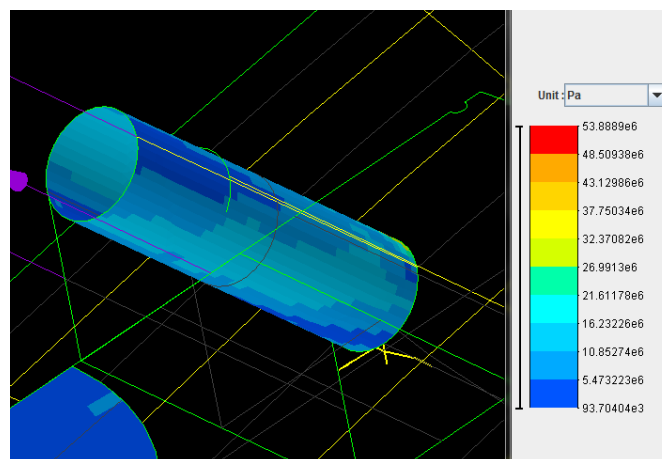
Figure 3.39: von Mises equivalent stress at the bottom of the aluminum cylinder

3.5   Validation of the Finite element model

Thanks to those tests, the finite element model can be assumed to be representative of the reality. As expected, the composite bar is undergoing a lot of efforts as well as the support. Some precautions needs to be taken while placing the rivets to avoid the propagation of microcracks. As the deformations of the finite element model are close to the one found with the experimental tests, the model is validated.

Chapter 4

Flight simulation

As all the geometry is known and the finite element model has been validated, the last step is to study the behavior of the drone during the flight. To do that, the Software PanAir is used to compute the pressure which will be applied on the plane to simulate a flight configuration. In order to find which flight configuration produces the highest loads on the plane, the gust envelope has to be computed. Some aerodynamic data are needed to compute it so the results obtained thanks to an experimental test in the wind tunnel are used. From the gust envelope, the load factors are calculated and the aerodynamic loads can be found. This method will give us the lift to produce to balance the load factor and will give us the angle of attack α of the plane. The angle of attack and the speed found with this method are inserted in PanAir to compute the distribution of the pressure on the drone. Eventually, the pressures and the load factor are applied on the finite element model to compute the stresses and the deformation that the plane is undergoing.

4.1 Introduction to PanAir

PanAir is a software developed by the NASA in the 90's to predict inviscid flows by using a high order panel method. As our drone will fly at low speed and has a simple configuration, the program should give a great overview of the real aerodynamic forces applied during the flight. As the program allows to study the flows proprieties for an inviscid fluid, the lift should be close to reality but the viscous component of the drag will be missing, only the induced drag is computed. The induced drag (D_i on the schema) is represented at figure 4.1. It is created because there is an angle difference (α_i) between the free steam direction (V_∞) and the effective direction of the airflow (V_{eff}) for a 3D wing. The missing component of the drag is not a real problem as the forces induced by drag are way smaller then the lift's ones.

With the hypothesis made by PanAir, the stall will not be represented which means that we must care of the results for the high angle of attack.
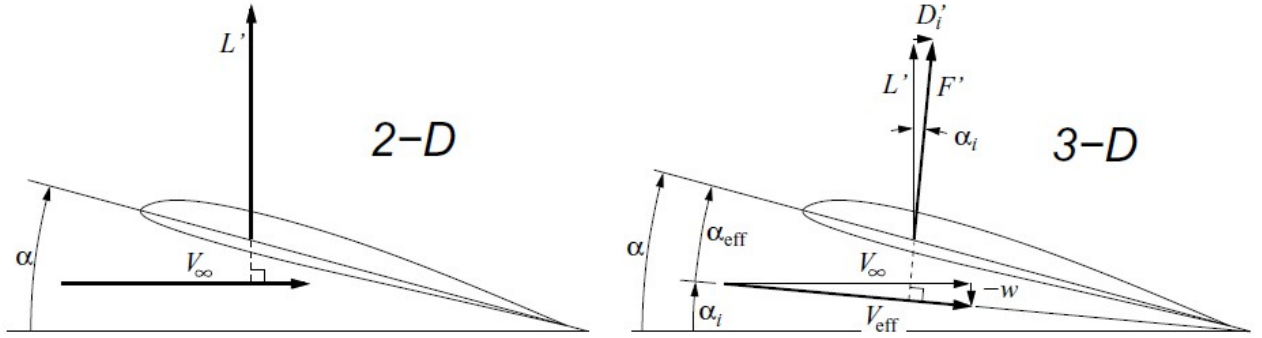
Figure 4.1: Schema of the induce drag

The method used by PanAir to solve the problem is explained below. The explanation is inspired by the documents of the NASA [1][2] written by Mr Larry Erickson and Mr Forrester Johnson.

It makes the hypothesis that the flow is inviscid, irrotationnal ($\overrightarrow{\nabla} = 0$) and steady ($\frac{\delta}{\delta t} = 0$). Considering a potential flow ($\overrightarrow{\nabla}\phi = \overrightarrow{V}$) leads to the Lagrange equation: $\overrightarrow{\nabla}^2\phi = 0$ where ϕ is the velocity potential and $\overrightarrow{V}$ is the velocity of the flow.

The software solves the Prandtl-Glauert equation which is $\overrightarrow{\nabla}^2\phi = (1-M_\infty^2)\phi_{xx}+\phi_{yy}+\phi_{zz} = 0$ where M_∞ is the free steam velocity. This equation is the easiest way to model an incompressible flow, the equation results of the general Navier-Stokes equation by neglecting the viscous effects, the heat transfers and considering an irrotationnal steady flow.

Two solutions of the Prandtl-Glauert equations are used and can be verified by direct substitution:

The first one is the point source : $\phi_P^S = -\frac{1}{R(\overrightarrow{x}_r,\overrightarrow{x}_q)}$

The second one is the point doublet : $\phi_P^D = \widehat{n}.\frac{-\overrightarrow{R}(\overrightarrow{x}_r,\overrightarrow{x}_q))}{R^3}$

Where R is the hyperbolic distance given by: $R = \sqrt{(x_Q - x_P)^2 + \beta^2 * ((y_Q - y_P)^2 + (z_Q - z_P)^2)}$

with $\beta = 1 - M_\infty^2$, in the case of incompressible flow, R is simply the geometric distance between the two points.

In those expression, x_P is the influenced point, x_Q is the point of influence where the source or the doublet is located.

In the case of low speeds , the velocity potential of the point P can be expressed as a function of the influencing panel Q such as :

$$\phi_P = \int \int_S (\sigma K_\sigma + \mu K_\mu) dS_Q \tag{4.1}$$

Where $K_{sigma} = \frac{1}{k}\phi_P^S(\overrightarrow{x}_Q)$ and $K_\mu = \frac{1}{k}\phi_P^D(\overrightarrow{x}_Q)$

In our case $k = 4\pi$ because the free steam velocity is way smaller than the speed of the sound.

From the value of the ϕ_Q and its definition, we find:

$$\overrightarrow{\nabla}_P \phi_P = \overrightarrow{v}_P = \int \int_S (\sigma \overrightarrow{\nabla}_P K_\sigma + \mu \overrightarrow{\nabla}_P K_\mu) dS_Q \tag{4.2}$$

$\overrightarrow{V}$ can be computed for each panel as the sum of the free steam velocity and the influence of the panel j, note that from the previous equation, the v_{ij} are expressed as a combination of the ϕ_P^S and ϕ_P^D:

$$\overrightarrow{V}_i = \overrightarrow{V}_\infty + \sum_j^N \overrightarrow{v}_{ij} \tag{4.3}$$

As the panel of the wing are impermeable, a condition of impermeability imposes that the component of the speed perpendicular to the panel must be null:

$$\overrightarrow{V}_i \cdot \dot{n}_i = (\overrightarrow{V}_\infty + \sum_i^N \overrightarrow{v}_{ij}) \cdot \dot{n}_i = 0 \tag{4.4}$$

$$\Rightarrow \sum_i^N \overrightarrow{v}_{ij} \cdot \dot{n}_i = -\overrightarrow{V}_\infty \cdot n_i \tag{4.5}$$

This equation written for all of the panels constitute a problem which can be written under a matrix of the type: $\mathbf{Ax} = \mathbf{b}$ where $\mathbf{x}$ are is the unknown and contains the parameters of the doublet and source singularities. After solving this problem, the value of $\mathbf{V}$ for each panel can be computed thanks to equation 4.3. From the value of $\mathbf{V}$, the pressure can be computed.

However, neglecting the viscous effect leads to a non-unique solution of the equation, this is why the wake at the trailing edge has to be explicitly chosen by the user, it consists in the Kutta condition. The position of the wake is easy to find as the UAV studied is a blended winged body. The wake is just assumed to be flat and it is starting at the trailing edge of the wing. This task is not possible when working with a fuselage as there is no real trailing edge. In our case, the part where the engine is located doesn't have a sharp trailing edge. The geometry chosen for the aerodynamic study is slightly changed to allow the creation of a wake at this spot. The problematic part is shown at figure 4.2 and a trailing edge is created. It will change the aerodynamic forces on the fuselage but as the part of the plane which has been changed is small compared to the span, it will only have a small consequences on the general results. However, we can expect an overestimation of the lift as the surface created has a profile which is much more likely to provide lift.
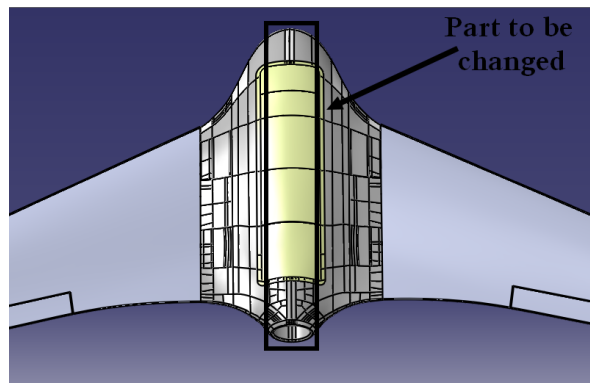
Figure 4.2: Part of the drone which has to be changed

The new geometry is shown on the figure below :
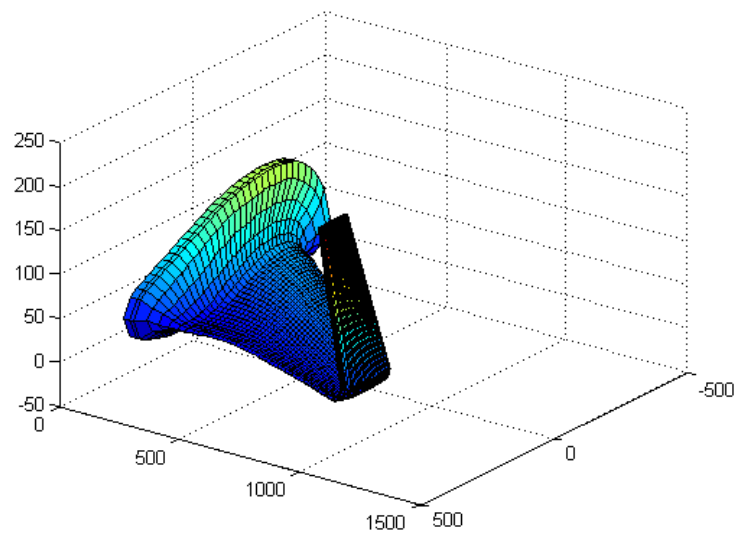
Figure 4.3: Geometry studied in PanAir
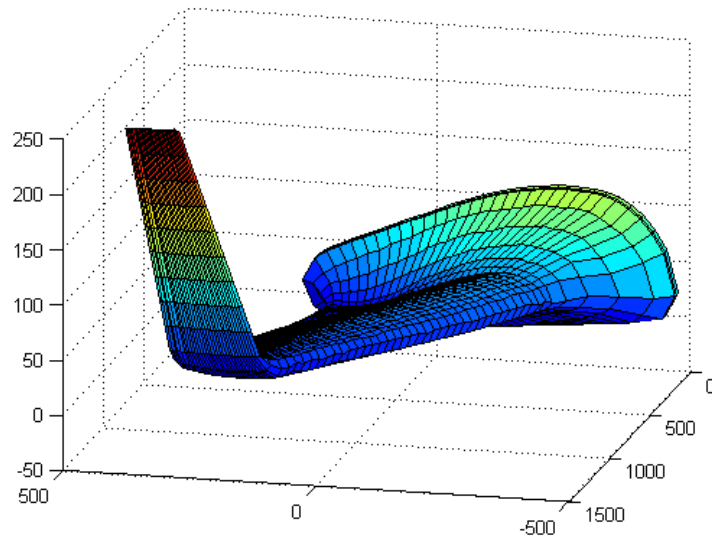
Figure 4.4: Geometry studied in PanAir

4.2 Geometry

As explained before, the geometry had to be changed to create a wake which start at the trailing edge of the wings. In order to do that, the section just before the location of the engine is selected and placed instead of the problematic point.

The definition of the geometry in PanAir is implicit, it means that the points needs to be given to the software in a certain order and the order will define the geometry. As we are working on a blended winged body aircraft, the usual way to do it is to give different slices of the aircraft along the span. In the same way it has been done for the finite element model, the symmetry of the aircraft is used and only half of it is represented. This is allowed in this case as we don't consider any sideslip effect. Then the different airfoils from the middle of the drone to the wing tip are inserted in PanAir. The points of the airfoils are encoded in a certain order too in order to define the good normal to the surfaces created. The first point is located at the trailing edge, then we travel through the extrados until we reach the leading edge and travel back through the interados to finally reach the last point which coincides with the starting point. A representation of the process is shown at figure 4.5 and 4.6.
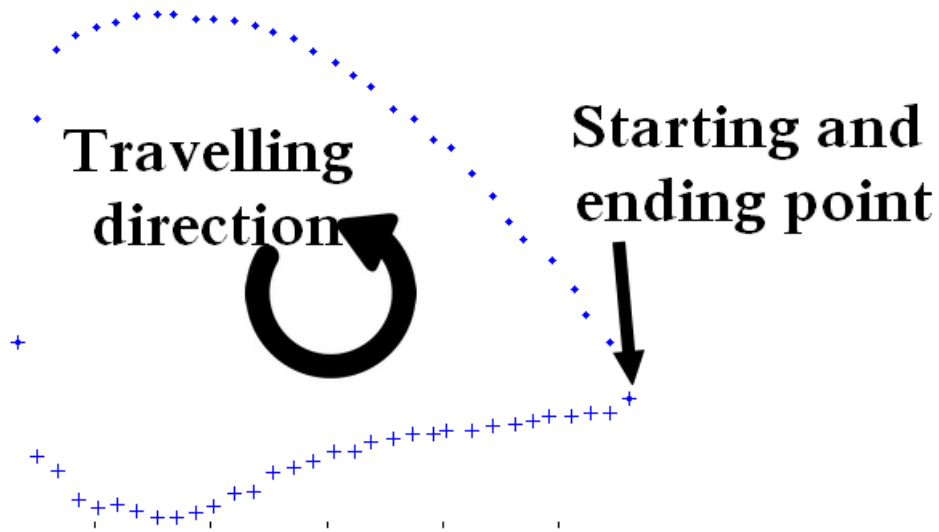
Figure 4.5: Order of the points given to PanAir
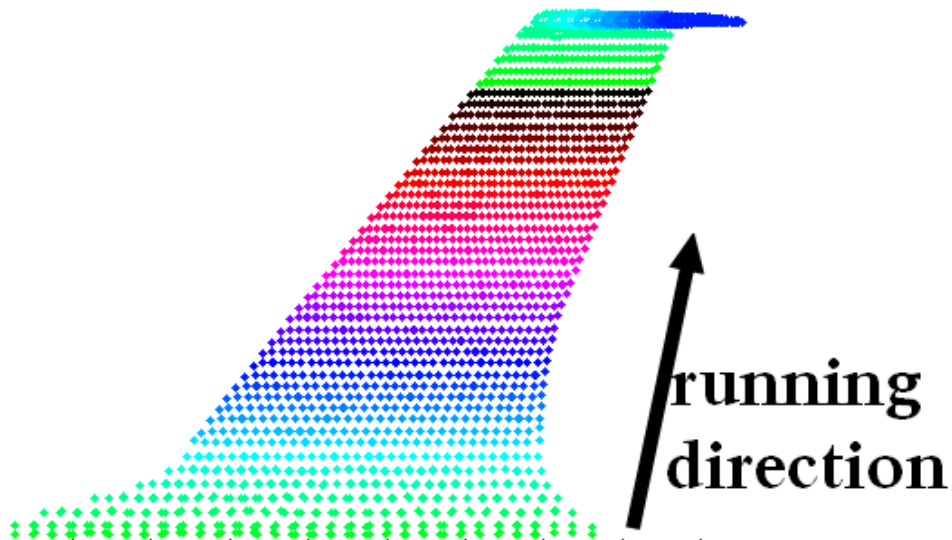
Figure 4.6: Order of the points given to PanAir

In the code, it is necessary to specify how many points are used for each airfoils (denoted as nm) and how many slices are used while traveling through the span (denoted as nn). The total amount of points given to the software is obviously equal to $nn * nm$, in our case, a great compromise between a fast resolution and a great convergence of the results is to use 55 slices (nn=55) and 63 points for each airfoils (nm=63).

It is hard to generate such a mesh automatically with a software. It has been tried on Samcef and GMSH but the results were not satisfying. For the same reason the initial CAD model had to be changed in the previous chapter, the meshing software always places a node at each end of the edges and this lead to a chaotic mesh while the one needed here has to be very regular.

The best solution to this problem is to use a meshing software to generate a mesh with a huge number of points (the more points are generated, the best the results will be). The generated points are post-processed in Matlab to generate manually the desired mesh. The mesh of the fuselage and the wing are generated apart to improve the processing time in Matlab. Samcef is used to generate the meshes and 250.000 points are generated for the wing and 280.000 for the fuselage.

The points are generated for the wing and the winglet quiet easily. The points of the fuselage are chosen by taking care to give the right profile at the middle of the fuselage. The generated mesh is shown at figure 4.7.
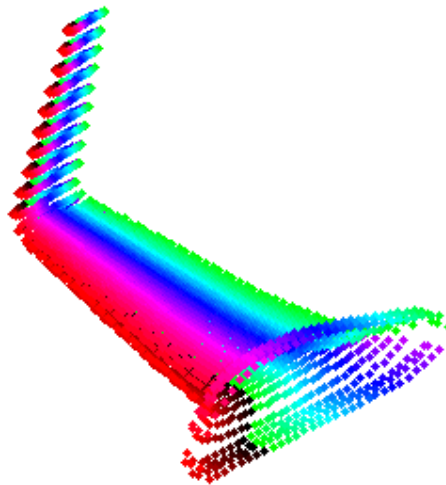
Figure 4.7: Mesh of the drone generated

A last problem remains, by importing the CAD files in Samcef, the geometry of the objects remained correct but the system of axis had been changed. The consequence is that the fuselage and the wing are not aligned anymore, the translation is easy to fix but the fuselage needs to do a rotation around its Y-axis to correspond to the 0 degree angle of attack of the wing.

The rotation is done by multiplying the coordinates of each node of the fuselage ($\mathbf{x} = (x_1, x_2, x_3)^T$) by a rotation matrix:

$$\mathbf{x}_{new} = \mathbf{R}_y(\theta) * \mathbf{x}_{old} \tag{4.6}$$

Where

$$\mathbf{R}_y(\theta) = \begin{pmatrix} cos\theta & 0 & sin\theta \\ 0 & 1 & 0 \\ -sin\theta & 0 & cos\theta \end{pmatrix} \tag{4.7}$$

The final set of points are found and displayed at figure 4.8.
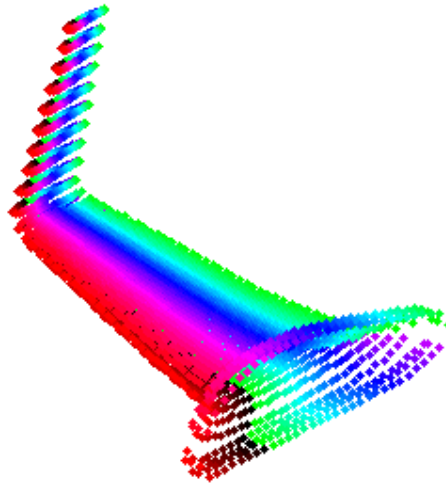
Figure 4.8: Final mesh of the drone for the aerodynamic study

The surfaces created and used by PanAir during the resolution of the equations can be modeled too and has already been shown at figure 4.3 and 4.4.

4.3   Test in the wind tunnel

Before computing the maneuver and the gust envelope, some experimental results can already be introduced. The first prototype of the UAV has been tested in 2015 in the wind tunnel of the University of Liege by Mr Andrianne. The main results that the tests have underline is the evolution of the lift in function of the angle of attack.

In the domain of the aerodynamic, it is more common to represent the 3D lift coefficient instead of the lift its self. The 3D lift coefficient is define as:

$$C_L = \frac{L}{0.5\rho V^2 S} \tag{4.8}$$

Where L is the lift, ρ is the density of the air at the altitude of the drone, V is the speed of the drone, S is the projected surface of the wing.

The curves found is shown below, note that C_D is the drag coefficient and is define in the same way than the lift coefficient: $C_D = \frac{D}{0.5\rho V^2 S}$ where D is the drag. The percentage in the legend correspond to the power of the engine.
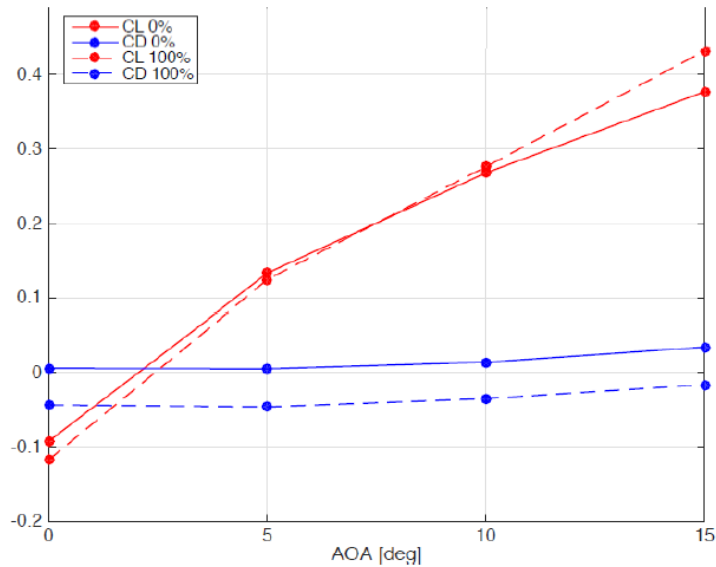
Figure 4.9: Experimental curves of the lift and the drag coefficients in function of the angle of attack

When the tests had been performed, the value of S wasn't known as the plans of the drone weren't available. Mr Andrianne decided to define S has : $S = bl = 1.54m^2$ where b is the span of the drone and l is the length of the fuselage. Thanks to the 3D model of the drone the real surface aera can be computed and is equal to $0.738m^2$. The real lift coefficient can be computed as $C_{Lreal} = C_{Lold}\frac{1.54}{0.738}$. We can see on the graph of the figure 4.9 that the lift coefficient changes a little bit when the engine is working, two reasons can explain it. The first one is that the propeller is perturbing the flow. The second one is that the engine can produce a resultant force with a component along the Z-axis not equal to 0. Indeed, in order to compute the lift coefficient, a sensor measures the vertical force produced by the plane. At rest, the sensor only measures the weight of the plane but when an air speed is set, it can measure the difference of the force and compute the lift. The lift coefficient is computed from the lift thanks to the formula of C_L. If the sensor is measuring the vertical force, then changing the angle of attack of the drone changes the orientation of the thrust produced by the engine and a component along the Z axis is added to the lift. For this reason, the value of C_L at 0% is used.

The new curve of the C_L can be computed and is shown at figure 4.10.
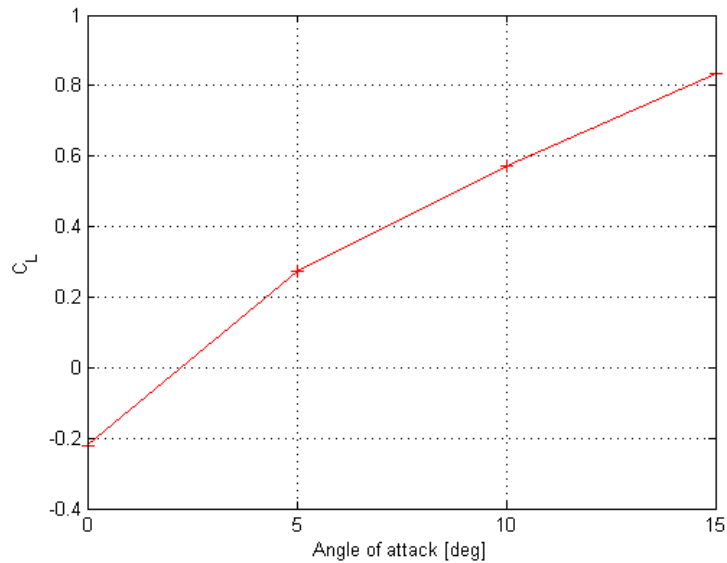
Figure 4.10: True experimental curves of the lift coefficients in function of the angle of attack

This curve will be used to verify the results found with PanAir. We can notice that the plane has a negative lift coefficient for an angle of attack of 0 degree and the lift is null for an angle of attack of 2.2 degree (denoted α_0). The value of $C_{L\alpha}$ can be computed as the mean slope of the C_L-angle of attack curve and is equal to 5.0.

4.4 Maneuver and gust envelope

In order to know the flight configuration we will study, the gust envelope has to be computed. The aerodynamic load highly depends of the speed and the angle of attack of the plane. Both of those parameters must be known in order to compute an accurate aerodynamic study.

4.4.1 Maneuver envelope

The maneuver envelope depends of a few factor:

- The load factor of the drone. This parameter is used to simulate the effect of the inertia of the drone in a static analysis. This is really interesting for us as it will be used in the finite element model. The maximum (n_{max}) and minimum (n_{min}) load factor are needed. Those parameters can be computed by using an analytical formula, however, this method gives results which doesn't make sense. This is probably due to the fact that we are working with a UAV. The FAR regulation provides statistical value and those are used here. The load can be set to $n_{max} = 4$ and $n_{min} = -2$.;

- The dive speed is also needed. This is also given by the FAR regulation, in the case of the Guardian Eye, it is set to $V_{dive} = 1.15V_{cruise}$, in our case, the cruise speed is about 90km/h, this leads to a dive speed of 103.5 km/h.

All of those parameters set the limit of the maneuver envelope which describes the limits where the plane can fly. This is shown at figure 4.11
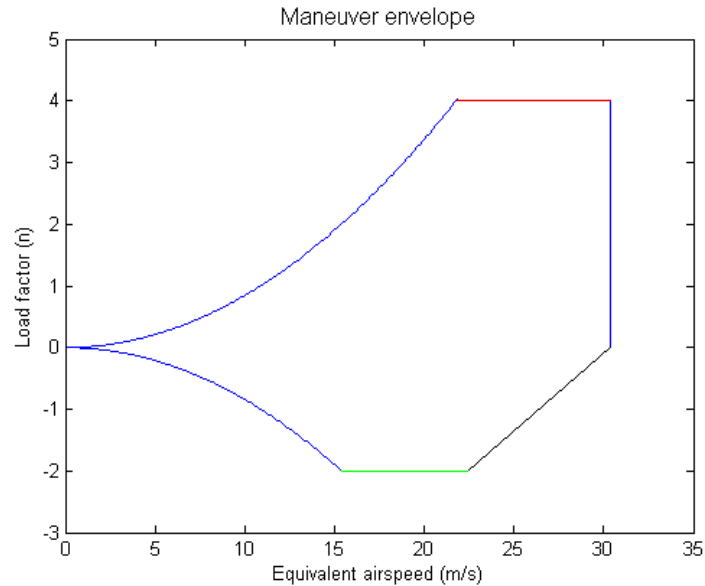
Figure 4.11: Maneuver envelope of the drone

Inside the envelope, the plane can flight safely.

A few zones are interesting, the left part of the graph is the zone where the lift is not high enough to balance the load factor applied on the plane, this is the stall limit. The limit of this zone is delimited by:

$$n = \frac{L}{W} = \frac{0.5\rho V^2 S C_{Lmax}}{W} \tag{4.9}$$

In this equation, most of the parameters have been introduced in the previous section and W is the weight of the plane.

Note that the C_{Lmax} which is the maximum 3D lift coefficient is known from the tests done in the wind tunnel and cannot be computed with PanAir as the stall effect can't be quantified. It is fixed to 0.85 for an angle of attack of 15 degree. This angle of attack is high but it has been verified experimentally that the drone doesn't stall at this speed, hence the value of C_Lmax is probably underestimated.

If the plane travels faster, we are located in the right zone and the load factor is the limiting factor, we must take care that it doesn't cause any structural damages.

We can notice that this maneuver envelope is a bit more restrictive than the real one. Indeed, the maximum lift coefficient which has been chosen is the maximum lift coefficient that has been measured in the wind tunnel. However, we are not sure if this coefficient keep growing for a

higher angle of attack. The load factor would have increase faster if a higher lift coefficient had been used.

An experimental test in the wind tunnel could be performed to find the real C_{Lmax} and the angle of attack corresponding to the stall of the aircraft. As we saw, the panel method used by PanAir doesn't allow to compute the stall speed. The analysis done here is limited by this value of C_Lmax.

4.4.2 Gust envelope

The gust envelope is another envelope which takes the effect of the gust into account. Indeed, if a wind gust is blowing on the aircraft, the flow perceived by the aircraft is changed which results in an increase or a decrease of the effective angle of attack. The gust envelope can be computed and it will be used to calculate the aerodynamic loads. The modification of the angle of attack is hard to calculate, hence, the FAR regulation define that the load factor of the gust envelope is delimited by:

$$n = 1 + \frac{k_g V_{gust} V_{plane} C_{L\alpha} \rho S}{2W} \tag{4.10}$$

Where k is the gust alleviation factor and μ is the airplane weight ratio, they are given by:

$$k = \frac{0.88\mu_g}{5.3 + \mu_g} \tag{4.11}$$

$$\mu = \frac{2W}{\rho MAC C_{L\alpha} S} \tag{4.12}$$

V_{gust} is the speed of the gust, this is given by statistical values and are shown is the table below:

	$V_{plane} = \pm V_B$	$V_{plane} = \pm V_{cruise}$	$\pm V_{dive}$
$V_{gust}[m/s]$	20.11	15.25	7.5

Eventually, $C_{L\alpha}$ is the slope of the 3D lift coefficient in function of the angle of attack and is computed thanks to the experimental tests.

The gust envelope of the plane can be computed and is shown below:
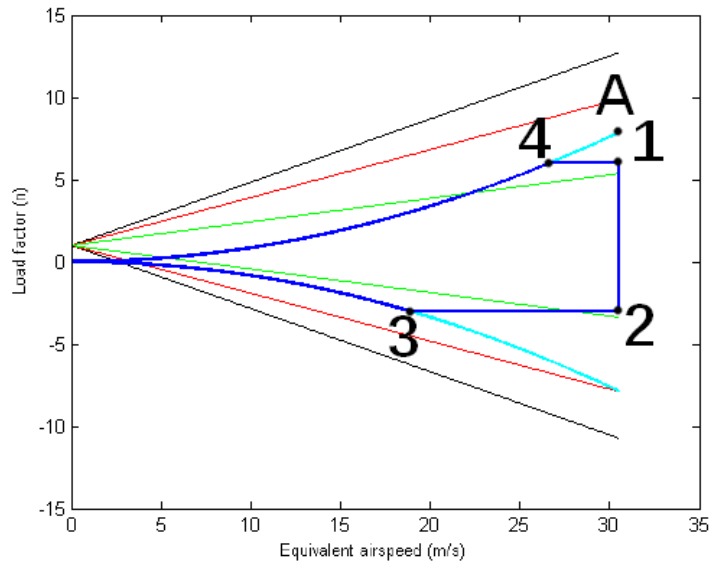
Figure 4.12: Gust envelope of the plane

We notice that the curve for $V_{gust} = 20m/s$ intersects the stall curve for a speed higher then the dive speed and this lead to a huge load factor when the plane is diving. However, the load factor is limited to a maximum value of 6. The plane shouldn't undergo a higher load factor. If we take the example of the acrobatic aircraft which are undergoing the highest load factor, n takes a maximum value of 6. For the same reason, the minimum value of the load factor is set to -3. As for the maneuver envelope, the value of C_{Lmax} doesn't allow the stall curve to grow fast enough to intersect the curves of n_g which limits our analysis.

The instant when the drone undergoes the highest loads should be when it reaches the point 1. At this point, the load factor is maximum as well as the speed.

We can compute the values of the aerodynamic loads for the interesting point of the envelope.

4.5 Aerodynamic loads

By knowing the loads factor at each point of the envelope, it is now possible to calculate the aerodynamics loads. The aerodynamic loads are calculated by resolving the equilibrium equation of the plane. The figure 4.13 shows all the forces that are acting on the plane during a resource.

Figure 4.13: Schema of all the forces applied on the plane during a resource

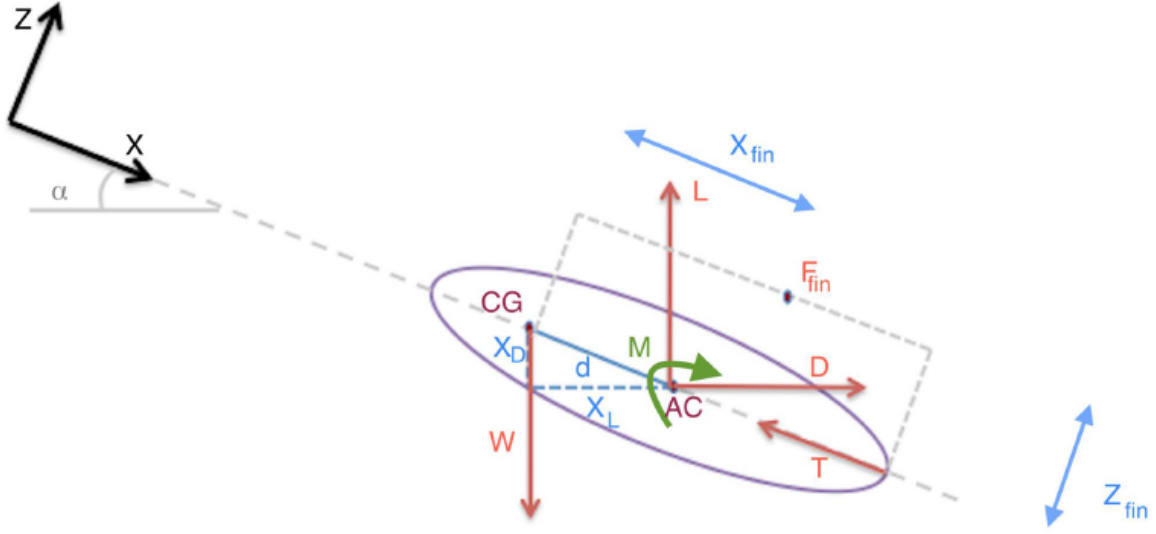The equilibrium equations (of the moment around the center of gravity and the vertical stability) can be written as:

$$-x_L L - x_d D + M = I_\theta \ddot{\theta} \tag{4.13}$$

$$L + T sin(\alpha - i_\omega) - nW = 0 \tag{4.14}$$

$$L = 0.5 \rho V^2 S C_{Lalpha}(\alpha - \alpha_0) \tag{4.15}$$

In this equation, I_θ is the first moment of inertia of the plane along the Y-axis, i_ω is the inclination angle of the propeller which is null as the thrust is directed through the center of gravity. $\ddot{\theta}$ is the maximum pitching acceleration allowed, it is imposed to 1.745 rad/s^2. T is the thrust produced by the propeller.

As we can see on the schema 4.13, the distance x_L and x_D depend on the angle of attack and the position of the aerodynamic center (center of application of the lift). However, those distances are hard to find as the geometry of the drone has been inspired by another one, the airfoil section are not known and the position of the aerodynamic center is unknown. This problem is solved by the fact that we are working on a blended wing body aircraft. In order to be stable in flight, this kind of aircraft needs to have its aerodynamic center almost superposed with the center of gravity. This configuration allows to have a moment around the Y-axis almost equal to 0 all the time and as a consequence, the usage of elevators is not needed. By making this hypothesis, we can assume that the distance x_L and x_D are equal to 0.

The schema at figure 4.13 is a simplification of the equilibrium of a classic plane. All of the forces applied on the tail are ignored as we are working with a blended wing body. The plane can be seen as a single wing without fuselage as the whole surface of the drone contributes to the lift. Eventually, the propeller is aligned with the center of gravity so that the angle i_ω is equal to 0.

This system of equation can be computed for a few points of the envelope. The values found are displayed below:

	n_g	Lift [N]	α [rad]
Point 1	6	336.18	0.214
Point 2	-3	-172	-0.080
Point 3	-3	-171	-0.17
Point 4	6	336.92	0.268

Figure 4.14: Aerodynamic loads at the points of the gust envelope

We can see that the drone undergoes the highest load at the point 1. The aircraft is flying at a speed of 30.3 m/s, the resulting lift is about 337 N, the load factor is equal to 6 and the corresponding angle of attack is equal to 0.266 rad=15.22 degrees.

This configuration is the one chosen to be studied in PanAir and on the finite element model as it is the moment when the loads applied on the drone are the highest. As we saw, the lift will be slightly overestimated for this angle of attack as the stall is not modeled in PanAir.

4.6 PanAir simulation

A summary of the input data given to PanAir are shown below:

Angle of attack	0-5-15 degree
Velocity	$0.09 * V_{sound}$
Points per section	55
Number of section	63

The simulations are run for an angle of attack of 0, 5 and 15 degrees. Those angle of attack are chosen to plot the C_L-angle of attack curve and verify that the results given by PanAir are close to the experimental tests in the wind tunnel.

An important remark has to be made, after a few tests, it has been noticed that the geometry given to PanAir corresponded to an angle of attack of about 3 degrees. This problem has been introduced during the importation of the geometry in Samcef. The problem is exactly the same that occurred with the fuselage which didn't have the same angle of attack than the wing. This easiest way to solve this problem is to run PanAir for the angle of attack of -3, 2 and 12 degrees which correspond in reality to the selected configurations of 0, 5 and 15 degrees. This problem could have been solved by applying a rotation to the set of points in Matlab but exporting the data in PanAir is a complicated task. The easiest solution is the one which have been chosen.

The results found on PanAir can be compared to the results found with the experimental tests in the wind tunnel. The C_L-angle of attack graph gives a great overview of the correlation of the model and the real tests. This graph is shown at figure 4.15. The experimental results are shown in red while the PanAir results are shown in blue.
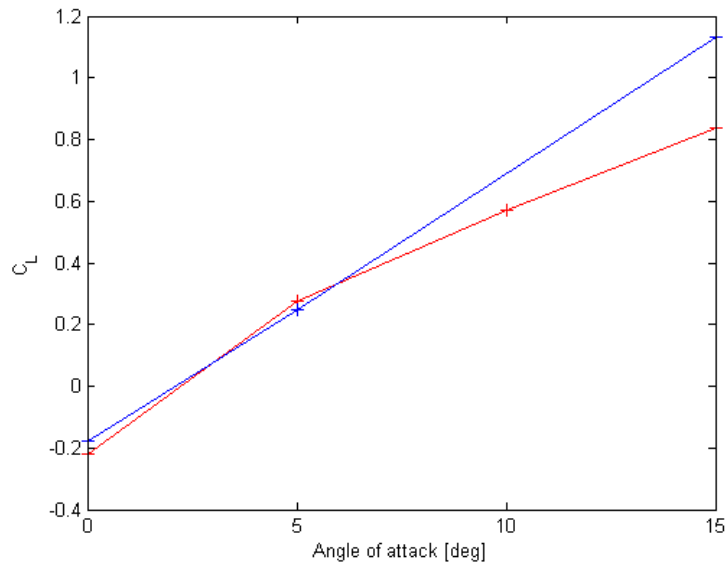

Figure 4.15: Comparison of the C_L-angle of attack curves between the PanAir simulation (in blue) and the experimental tests (in red)

We can see that the aerodynamic model is really close to reality for a small angle of attack. This result is satisfying. However, we didn't expect PanAir to work well for high angle of attack. For a high angle of attack, the lift is overestimated by PanAir.

Note that the overestimation of the lift for a high angle of attack is probably because in reality, a part or the whole the wing is starting to stall which is not the case in the PanAir model. As the airfoil of the wing is different over then span, it is possible that a part of the wing starts to stall while the other parts are still producing lift.

Eventually, PanAir allows us to extract all of the pressures coefficients of each surfaces created. Those pressures coefficients are useful as they allow us to computed the pressure which will be applied on the finite element model to simulate the aerodynamics loads.

Chapter 5

Structural analysis in flight conditions

In this last part, all of the parameters determined before are applied on the finite element model. It allows us to see how the drone reacts when it is performing a resource at the point A of the gust envelope.

5.1 Influence of the inertia

As it has been said before, a dynamic phenomenon is simulated on a static model. The load factor is used to take the effect of inertia into account. In the case of a resource, the load factor is high (n=7.85), and the weight of the drone has to be multiplied by n. In the finite element model, this is done by multiplying the gravitational acceleration by the load factor. In this part, the simulation is done for a flight configuration which means that the real mass of the drone has to be used. For now, the mass of the drone on the model was simply equal to the mass of the structure as the experimental test of the fuselage had been done without payload. In this last part, the mass of the payload has to be added to reach the real mass of the drone (6 kg). Those components can be modeled simply by adding some mass inside the fuselage. The best option would have been to add a mass distributed on the bottom of the fuselage. Unfortunately, this option is not available in Samcef and a surface force is used on the bottom of the fuselage. The resultant of this force is equal to $nM_{add}g$ where n is the load factor, M_{add} is the mass to add and g is the gravitational acceleration. We decided to add a load which correspond to 2kg to reach the 6kg configuration that has been used to compute the aerodynamic loads.

5.2 Application of the aerodynamic forces

The aerodynamic forces can be applied by applying the pressure computed by PanAir.

PanAir actually doesn't return the pressure itself. It gives us the value of the second order pressure coefficient (C_P). The pressure can be computed from the C_P thanks to the formula:

$$C_P = \frac{p - p_\infty}{0.5\rho_\infty V_\infty^2} \tag{5.1}$$

In this equation P is the pressure over panel, p_∞ is the pressure in the free steam, ρ_∞ is the density of the flow in the free steam and V_∞ is the velocity of the fluid in the free steam.

The pressure can't be applied directly from the output file of PanAir to Samcef. In Catia such a process is easy to do as it is possible to convert the pressure into a series of resultant forces and project them on the model. This process is not possible in Samcef. In order to solve this problem, the surface of the wing and the fuselage are cut into smaller surfaces. In our case, there are 10 divisions along the span and 5 divisions along the chord, this gives a total of about 100 surfaces. A pressure is then applied on each surfaces. The pressure applied on a surface is equal to the sum of the pressure found with PanAir averaged by the area of their surface of application.

The accuracy of the result depends on the number of surfaces used in Samcef. If we consider an infinite number of surfaces, the configuration will be the same as than the one given by PanAir. In our case, a good compromise is to use a total of 100 surfaces as it is shown at figure 5.1. Using more surfaces could be done but the time needed to enter each pressure of each surface is really long.
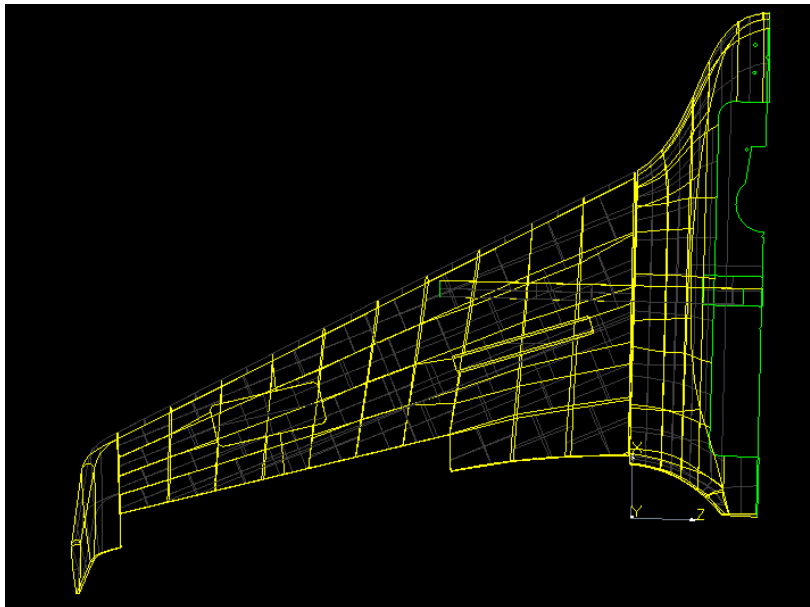

Figure 5.1: Surfaces used to apply the pressure

5.3   Boundary conditions

The right choice of the boundary conditions is really important. The flight conditions are hard to model so in our case, the middle of the plane has been clamped. Those boundary conditions remove the rigid body modes and allow to study the plane in a configuration close to the flight conditions.

5.4   Results

We can take a look at the nodal displacements. They are shown at the figure 5.2. We can see that the wing is deflected upward due to the lift. In deed, most of the weight of the fuselage
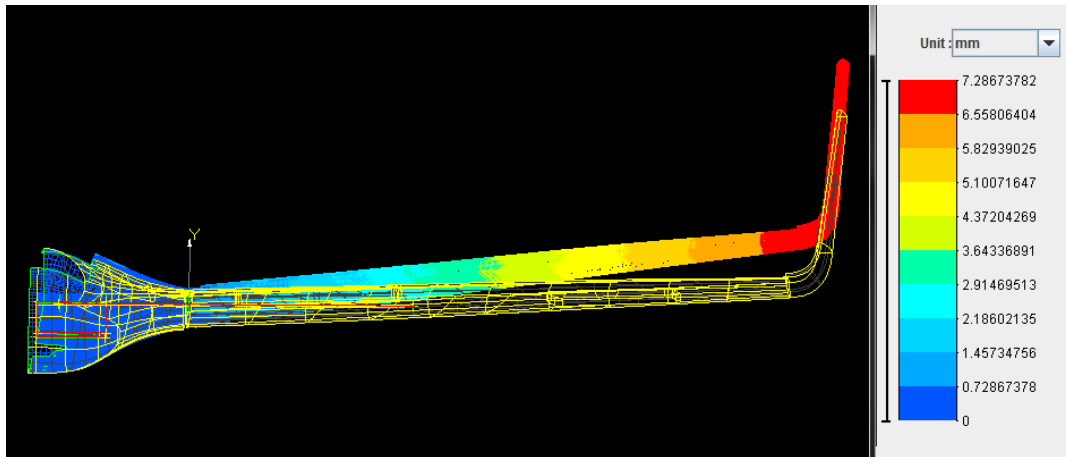
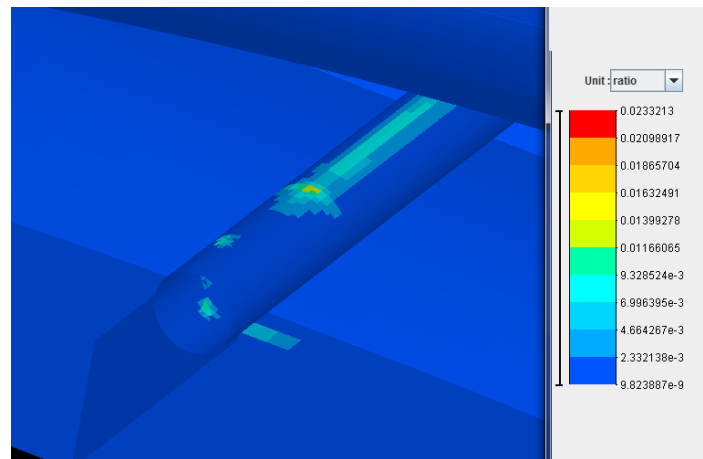Figure 5.2: Displacement of the wing in flight conditions

Figure 5.3: Value of the Tsai-Hill in the composite bar

is located near the fuselage while most of the lift is produced by the wings. The displacements found are small (7mm) and the deformations should not change the aerodynamic behavior of the plane.

The value of the Tsai-Hill can be analyzed too.

The composite bar is undergoing tiny stresses which is characterized by a Tsai-Hill value close to 0 (0.02) and far from 1. This is shown at figure 5.3. However, as the inertial forces and the lift are almost in equilibrium, we can understand that the bar doesn't need to carry a lot of efforts as it was the case during the experimental test of the chapter 3. Therefore, the resulting stresses are small.

We also notice that the bottom of the fuselage and the support are characterized by a Tsai-Hill value really small too which wasn't the case in the bending test performed in the chapter 3. This
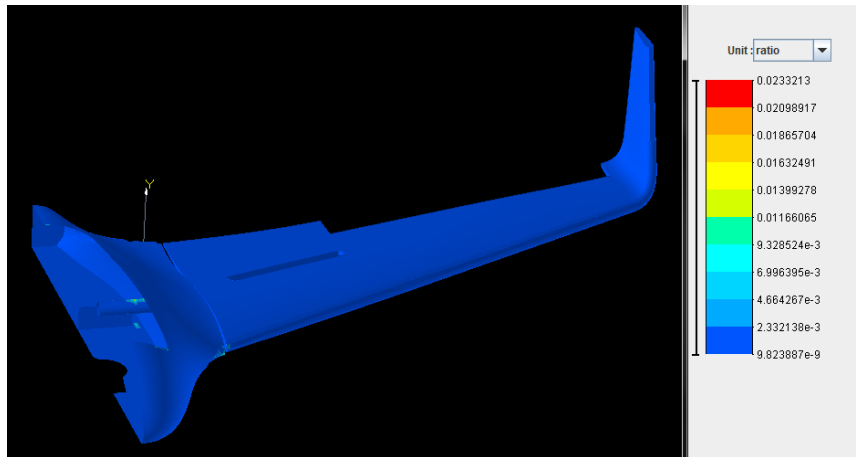
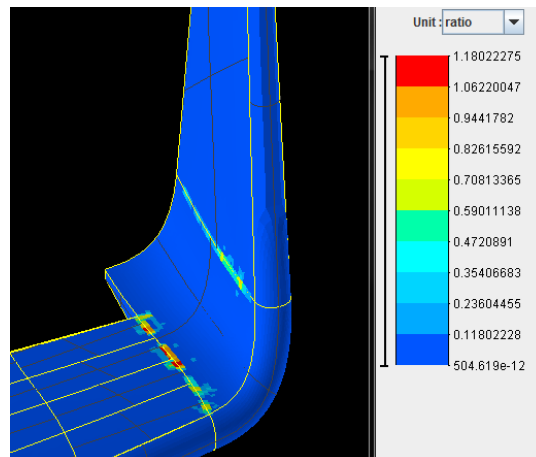Figure 5.4: Value of the Tsai-Hill for the skin

Figure 5.5: Value of the Tsai-Hill at the junction between the wing and the winglet

confirms the results found for the composite bar, the bar is not undergoing high stress and the stress transmitted to the support is small too.

The figure 5.4 shows the value of the Tsai-Hill for the skin of the wing and the fuselage. The Tsai-Hill values are very low every where as expected. In deed, the skin is very thick for such a small drone. However, using a thinner skin could increase the displacements which could change the aerodynamic proprieties of the plane.

During this simulation, high stresses were found at the junction of the wing and the winglet which was a strange result as the value of the Tsai-Hill values seemed to be chaotic and presented sudden changes. This is shown at figure 5.5. It was actually due to a numerical errors introduced by the software. As it was the case in the section 3.4, the software introduces artificial stresses to insure the continuity of the kinematic constrains between two different materials. It is solved by removing the gluing constrains between the foam and the skin at this spot.
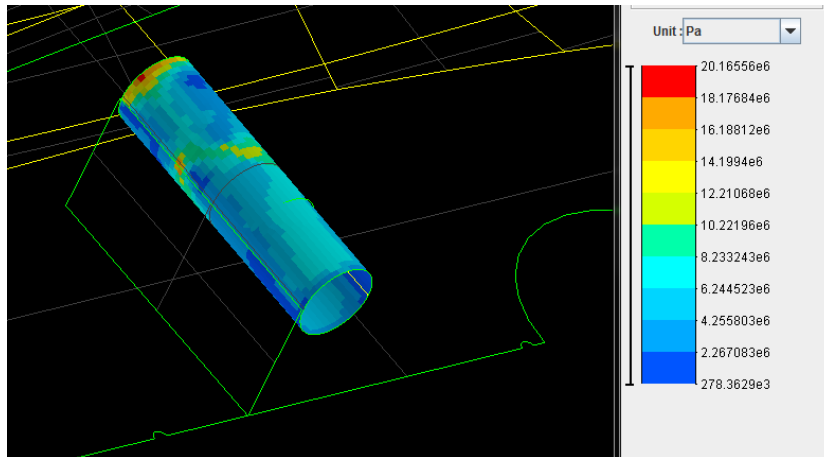
Figure 5.6: Value of the von Mises equivalent stress in the lower skin on the top of the aluminum cylinder

The value of the von Mises equivalent stress can be checked for the aluminum cylinder in order to see the magnitude of the efforts transmitted from the composite bar to the supporting cylinder. The results are shown at figure 5.6 for the lower skin which is undergoing the highest stresses.

We can notice that the maximum constrain is way smaller than the yield strength of the material (20 MPa while the yield strength is 240 MPa).

To sum up, the composite bar is undergoing the highest stress as expected. It is oversize compared to the size of the plane and the loads which are applied to it but it constitutes a great margin of security without adding too much weight.

The skin of the wing in every test remained far from its limit of elasticity then a diminution of the thickness of the skin of the wing could be considered in the future. This diminution of thickness would probably increase the deformations during the flight. A study could be done to check that those deformations don't change the aerodynamic proprieties of the aircraft too much.

Chapter 6

Conclusion

To sum up this whole project, we have been able to see the huge advantages that the composite materials has. It combines a high tensile modulus with a high strength for a density way smaller than the common alloys. Those advantages makes the carbon fiber composite one of the best material to use in aeronautics.

The three-point bending test performed has been very useful to verify the proprieties of the material provided by the manufacturer. However, this test could not verify the value of certain parameters such as the shear modulus or the Poisson ratio. Some other tests could be performed to highlights those proprieties. A tensile test could be performed with samples with fibers oriented in $+/45$ degrees.

The bending test of the real drone allowed to validate its finite element model. It has been noticed that the finite element model was a bit stiffer then the real plane which is explained by the fact that the model doesn't takes the rivets, the joints and the complex interactions between some elements into account.

The PanAir simulation were performed and compared to the results found in the wind tunnel. The PanAir simulation makes a small overestimation of the lift for high angle of attack which can be explained by two factors :
- Small changes in the geometry had to be done in order to attach a wake to the fuselage
- The PanAir simulation gives a lift for an attached flow while the real wing might have started to stall.

The final analysis of the flight conditions allowed to underline that the composite bar is the one which is undergoing the highest stresses. However, it remains far from its limit of elasticity. The skin of the wing in general is oversized but reducing its thickness might lead to too large deformations of the wings.

Chapter 7

Future works

During this thesis, a structural analysis have been done but this work could be pushed further.

The version of the drone studied is the first commercial version. Some modifications will be done in the next version such as the integration of the rudders on the winglets. This modifications will induce more loads on the winglet. The reaction of the structure to those new loads could be studies.

An aeroelastic analysis of the drone seems really interesting to do. Indeed, the interaction between the inertial, the structural and the aerodynamic forces can lead to dynamic instabilities such as flutter. Those kind of phenomenon can lead to high-amplitude vibrations which are dangerous for the structure.

The first feedback of the prototype of the Guardian Eye indicated that the winglets tend to vibrate a lot. Those vibrations can increase the stress on the winglet or lead to fatigue failure. A detailed aerodynamic analysis could also be done to reduce those vibrations. For example, a new geometry has been proposed by Martin Masereel in his Master Thesis which consists in reducing the size of the winglets.

The same kind of analysis which has been done in this project could be done on this new suggested geometry to check if the drone can undergo the new aerodynamic loads.

The society which is developing the drone is also interested in creating a smaller version of the drone which would be adapted to the wind tunnel of the University of Liège. Developing such a model can be interesting as it could be used to study the aeroelastic phenomenon.

In the last section of the analysis, it has been explained that the analysis of the aerodynamic loads was done for a drone traveling without a sideslip angle. The reduced model could be used in the wind tunnel to study the effect of the sideslip angle on the flow proprieties and the aerodynamic loads on the winglet.

References

[1] Erickson, Larry L.: Panel Methods - An Introduction. NASA Technical Paper 2995, December 1990.

[2] Johnson, Forrester: A General Panel Method for the Analysis and Design of Arbitrary

[3] Configurations in Incompressible Flows. NASA Contractor Report 3079, May, 1980. 2004 Lecture Notes. University of Aizu, Aizu-Wakamatsu 965-8580, Japan

[4] A5021 User's Manual-PAN AIR Technology Program for Solving Problems o/Potential Flow about Arbitrary Configurations

[5] L. Noels, MECA0028-1 Structures Aéronautiques (Aircraft Structures)

[6] Pre-Insulated Pipe Supports Online Catalog , http://www.pipingtech.com/products insulated-pipe-supports/technical/poly.htm

[7] Thomas Andrianne. Test report - Drone Vigano. Technical report, University of Liège, 2014.

[8] L. Noels, APRI0004-1 Aerospace design project

[9] Advanced T700/XB3585 UD carbon fibers-reinforced composite, Sorin Vlase, Universitatea Transilvania Brasov

[10] Fibre-epoxy composites at low temperatures, G. Hartwig and S. Knaak

[11] T700S DATA SHEET, Torayca

[12] Wit Witkiewicz*, Andrzej Zieliski** *Ship Design and Research Centre,Department of Materials Science, Corrosion and Environment Protection, Gdask, Poland, **Gdask University of Technology, Department of Materials Science and Engineering, Gdask, Poland,

[13]Project : Study of a UAV structure Authors : Charbon Cyril Delvoie Cedric Plumacker Florence Salbati Riad University of Liège